USING MULTI-AZIMUTH AND MULTI-POLARIZATION GROUND PENETRATING RADAR TO CHARACTERIZE A FRACTURED FAULT ZONE IN MASON COUNTY, TEXAS

A Thesis

by

AKHIL AMARA

Submitted to the Office of Graduate and Professional Studies of
Texas A&M University
in partial fulfillment of the requirements for the degree of

MASTER OF SCIENCE

Chair of Committee,	Mark Everett
Co-Chair of Committee,	Bobby Reece
Committee Member,	Chris Houser
Head of Department,	Mike Pope

August 2016

Major Subject: Geophysics

ABSTRACT

A multi-azimuth and multi-polarization ground penetrating radar (GPR) survey is carried out to help characterize a fractured fault zone located in Mason County, Texas. A total of 36 lines were acquired on and near the fault zone to try to identify the GPR signature of a complex fracture system. These lines were run through a standard set of processing steps to try to identify the fractures. The results showed that the multi-azimuth survey helped identify the dominant strike of the fractures, which was parallel to the strike of the fault (NE-SW). The multi-polarization survey helped identify the different fills of the fractures. Due to the orientation of the fractures, the PP orientation showed the resistive fractures while the TT orientation showed the conductive fractures.

gprMax, a 2-D finite-difference time-domain GPR simulation software, was used to confirm the results seen in the field data. Two 2-D models were created to understand the GPR response of the different fracture fills in the TT orientation. The first model simulated 3 identical fractures with 3 different fracture fills (air, water, clay). Results of this model showed that in the TT orientation, the air filled fractures have the weakest response while the clay filled fractures have the strongest response. The second model simulated the dominant fractures seen in Line A PP and TT orientations. The results again showed that in the TT orientation, conductive fractures have the strongest response while the resistive fractures have the weakest response, confirming the results from the field data.

A geophysical workflow was proposed to help identify buried shallow faults in remote locations. This workflow will help enhance the field observations of an area. The

workflow goes from surveying a large area (100s of m) using aeromagnetic data to identifying fractures in a fault zone at cm scale by using GPR method shown in this research.

DEDICATION

I dedicate this thesis to my parents Raghu and Radhika, and my sister Snigdha.

ACKNOWLEDGEMENTS

I would like to express my gratitude to my committee chair, Dr. Mark Everett, for taking me on as a student and allowing me to pursue my passion of field work, both as an undergraduate and graduate student. I greatly appreciate the opportunity he has given me and his assistance with this thesis project. I want to thank my committee member, Dr. Bobby Reece and Dr. Chris Houser, for their invaluable support and guidance through this project.

Thanks also go out to my friends and colleagues within the department who assisted me, including Patrick Wagner and Ivan Vazquez for help with fieldwork and data processing. Also, thank you to Mark Mitchell of Mason Mountain Wildlife Management Area for providing lodging and access to the field site.

Finally, I would like to thank my family for all their love and support through this incredible journey. They have been my source of motivation and encouraged me to always do better.

TABLE OF CONTENTS

Page

LIST OF FIGURES

1. INTRODUCTION

The goals of the research are two-fold: (i) to perform detailed subsurface structural imaging using ground penetrating radar (GPR) to characterize a fractured fault zone located in the western potion of the Llano Uplift, central Texas; (ii) to integrate the results of the GPR study with previous geophysical research on the same fault zone which hopefully can provide further insight into the geologic history of the Llano Uplift. To achieve the first objective it is necessary to understand the GPR signature of a fractured fault zone such as those produced by high angle normal faults present in the Llano Uplift. To image the Llano fractured zone as a specific case, a multi-azimuth and multi-polarization GPR survey was performed over a Pennsylvanian high-angle normal fault located within the Mason Mountain Wildlife Management Area (MMWMA) (Figure 1).

The Llano uplift is associated with several major deformation events, primarily the Precambrian Granville Orogeny (~1.2 Ga collision between the Laurentian and Kalahari cratons). Following this orogeny, a series of granitic plutons intruded ~1100-900 Ma (Merrill et al., 1991). A subsequent major geological event was the Ouachita orogeny that took place during the Pennsylvanian. This orogeny produced the large-scale normal faults seen in the area. The research area is characterized by good surface exposures of rocks indicating the presence of pervasive faulting. Undergraduate geology students at Texas A&M University have mapped this fault extensively over the past few years and many MS theses on the Llano Uplift have been written (e.g. Cohrs, 2012;

Harper, 2011; Murphy, 2014; Pereira, 2013). The surface geology has been mapped in great detail while the subsurface remains poorly understood.

Seol et al. (2001), Grasmueck et al. (2014) and others have shown that a multi-azimuth and multi-polarization GPR survey can be used effectively to map a single subsurface fracture by analyzing radar returns as a function of the transmit-receive (TX-RX) antennae orientation and the dip angle of the fracture. Since the receiver records only the component of the electric field that is aligned parallel to the RX-antenna long axis, a fracture that is oriented orthogonal to the RX long axis will generate a minimal GPR response (Grasmueck et al., 2014; Seol et al., 2001). Thus, GPR reflection energy is greatly affected by the strike and dip of the fracture. A multi-azimuth and multi-polarization GPR survey is able to illuminate fractures of arbitrary strike and dip. Due to the complexities of such a GPR dataset, forward modeling software is useful to help interpret the data. I have used gprMax for this purpose; it is an electromagnetic wave simulation software based on the finite-difference time-domain (FDTD) method (Giannopoulos, 2005; Warren et al., 2015). This software allows the user to simulate a fractured fault zone using the same acquisition parameters as were employed to collect the field data, thus allowing an accurate modeling representation of the field scenario.

The second objective of this project is to integrate the results of the GPR research on the Mason fault with other near-surface geophysical surveys that have been performed in the area. There have been three recent Texas A&M MS geophysics theses that have studied the same fault zone using various techniques including seismoelectric, magnetics and electromagnetic induction. A secondary focus of the present research is to

combine the GPR results with the previous geophysical information about subsurface fractures present within the fault zone.

The Llano Uplift has been affected by various episodes of structural deformation since the Precambrian. The hypothesis is that, within the multi-polarization and multi-azimuth GPR images, evidence of the various geological events will be present, including the extent of the fault damage zone. The results of the research should provide a better understanding of the geological evolution of the Llano Uplift. Additionally, I have suggested an integrated near-surface geophysics workflow that can be applied to other fault zones and shallow fractured reservoirs.

2. GEOLOGIC HISTORY

The field site is located within the Mason Mountain Wildlife Management Area (MMWMA) ~12 km north of Mason, Texas (Figure 1). The site is host to a graben that is bounded by a high-angle Pennsylvanian normal fault, which in turn is part of a larger system of faults (Figure 2, blue arrow) that trend northeast-southwest (Garrison and Mohr, 1983; Mosher et al., 2008). The hanging wall, located southeast of the fault slip surface, contains Middle to Late Cambrian age Hickory Sandstone; the footwall, located northwest of the fault plane, contains Precambrian age Town Mountain Granite. The footwall also contains Precambrian marble, an important component of the Packsaddle Schist formation.

2.1. Structural History

The Llano Uplift region has been shaped by several major deformation events since the Precambrian Grenville orogeny. The Mesoproterozoic Grenvillian collision between the Laurentia and Kalahari cratons, at the North American and African plate margins, contributed to the formation of the supercontinent Rodinia (Figure 3a, b) (Dalziel et al., 2000; Garrison and Mohr, 1983; Nelis et al., 1989). The Llano province was located along the southern margin of Laurentia within the Grenville orogenic belt extending from Texas to Scandinavia (Mosher et al., 2008). The orogeny caused regional NW-SE trend folding, which was followed by a series of granitic pluton intrusions ca.1100-900 Ma (Merrill et al., 1991). Several E-W and NW-SE regional strike slip fault systems formed in response to the intrusions (Figure 3c and Figure 4) (Garrison and Mohr, 1983). Post-tectonic intrusion of granites into the folded terrain may have been

caused by slab breakoff (Figure 3d) (Garrison and Mohr, 1983; Mosher et al., 2008). Sandstones were later deposited during the early part of the Cambrian-Ordovician marine transgression. These formations were then fractured and faulted during the Pennsylvanian perhaps in response to the flexural bending of the North American plate caused by the Paleozoic Ouachita orogeny, a continent-continent collision between North America and South America (Becker, 1985; Harper, 2011). These high-angle faults constitute the commonly observed NE-SW (Garrison and Mohr, 1983). Amsbury and Haenggi (1993) proposed an alternative theory that the fault motions are strike-slip caused by north-south compression. Their ideas stem from field observations and fault map patterns that show near-vertical faults with strike-slip displacements up to several km. This scenario changes the tectonic kinematics from one of extension to one characterized by a brief period of compression, resulting in a northward thrusting that formed the strike-slip faults (Amsbury and Haenggi, 1993).

2.2. Stratigraphy

The study site is located on the western margin of the Llano Uplift, which at present day is a broad structural dome of 2-3 km relief (Mosher, 1998). The uplift is comprised mainly of the Precambrian granite that formed during and shortly after the Grenville orogeny, as described above (Figure 4). The rock units of importance to this study are the Hickory Sandstone, Town Mountain Granite and Packsaddle Schist. Precambrian marble is found in conjunction with the granite and schist. The Hickory Sandstone is Middle to Late Cambrian in age (Figure 5) and comprised of fluvial, marine and shoreline transgressive strata characteristic of a shallow sea environment (Teran,

2007). The Hickory Sandstone is organized into three distinct units: The Upper, Middle and Lower that transition from shallow marine to fluvial deposits. The Lower Hickory Sandstone, resulting from a fluvial depositional environment, is exposed within the fault zone. The Town Mountain Granite is the basement rock that underlies much of the Hickory Sandstone. Town Mountain Granite formed due to the aforementioned magmatic intrusion and contains coarse-grained, pink plagioclase and quartz. The marble, exposed in the footwall of the fault, is assigned to the Honey Formation of the Packsaddle Schist Group (Becker, 1985; Harper, 2011).

2.3. Fault Geometry

Chester et al. (2004) classified fault zone structure into two main components: (i) the damage zone and fault core and (ii) the undeformed host rock outside the fault zone. Choi et al. (2015) further added a transition zone between the fault core and the damage zone (Figure 6). The boundary of a fault zone marks where the deformation intensity is reduced to the background levels of deformation, if any, within the host rock formations (Chester et al., 2004; Chester et al., 1993; Choi et al., 2016; Faulkner et al., 2003). The fault core comprises highly deformed rock that may contain cataclastic foliations and ultracataclasite layers, as shown in Figure 6. The surrounding damage zone is a relatively thick zone of fractures which may also contain folded strata, veins, and microfractures. The intensity of the fracturing decreases with distance from the fault core, becoming negligible at the undeformed host rock (Chester et al., 2004; Chester et al., 1993; Choi et al., 2016) (Figure 7).

2.4. Previous Geophysical Research

Several geological and geophysical studies focued on local faults have been conducted at MMWMA (Cohrs, 2012; Murphy, 2014; Pereira, 2013). These previous studies utilized various geophysical methods including seismoelectric, electromagnetics and magnetics.

Cohrs (2012) conducted a seismoelectric survey along the strike of a nearby fault zone that has similar geometry to the one under consideration herein. The objective of the study was to generate and analyze guided seismoelectric waves propagating within a fault zone. The results were then compared to data from a conventional reflection seismic survey. Cohrs (2012) showed that the seismoelectric and the seismic techniques produced comparable signals within the fault zone. The data exhibited guided waves in the form of higher amplitude late-arrivals compared to the normal amplitudes and arrival times of body waves propagating wholly within the surrounding lithologies (Cohrs, 2012) (Figure 8).

Pereira (2013) applied the magnetic method using a Geometric-G858 Cesium vapor magnetometer to refine the location of the fault that was previously mapped by Texas A&M geology field camp students at MMWMA. Processing and interpretation techniques such as diurnal correction, regional correction, reduction to pole (RTP) filtering, Euler deconvolution, forward modeling and inversion were employed to characterize the fault zone through its subtle magnetic signature. The study found that Euler deconvolution applied to RTP-filtered data best imaged the geological and

structural contacts (Figure 9). The results were then compared to previously acquired geophysical data, which supported the inferred location of the fault (Pereira, 2013).

Murphy (2014) conducted a tensor controlled source time-domain electromagnetic survey with the objective to characterize the fault at MMWMA. In this method, eddy currents are induced in the subsurface. Induced electromagnetic currents have been hypothesized to diffuse anomalously in the presence of a geologically rough medium such as the fractured subsurface of a fault zone (Weiss and Everett, 2007). The late-time transient electromagnetic response of a uniform geological halfspace exhibiting classical diffusion of currents decays with time according to a $t^{-5/2}$ power law. If the measured slope of the late-time transient response deviates from this power law, and the late-time transient response is linear on a log-log plot with some other slope, it may indicate anomalous diffusion in a uniformly rough halfspace. The responses measured by Murphy (2014) showed a faster late-time decay than $t^{-5/2}$ at long TX-RX offsets, labeled "superdiffusion" in Figure 10, which suggests the presence of highly resistive fractures within the geologically rough fault zone. Slower late-time decays, labeled "subdiffusion" in Figure 10 were inferred at near TX-RX offsets which indicate the presence of electrically conductive fractures closer to the surface (Murphy, 2014).

3. GROUND PENETRATING RADAR THEORY

Ground penetrating radar (GPR) is a non-invasive electromagnetic geophysical technique that has long been used extensively for many purposes, including geotechnical and transportation engineering, environmental site characterization, archeological investigations, cryosphere studies, and geological mapping (Milsom and Eriksen, 2011). GPR utilizes the propagation in subsurface geological media of an electromagnetic wave in roughly the 20 MHz – 4 GHz frequency range. One of the many reasons GPR is popular is due to its similarities with the seismic reflection method. While the seismic wavefield response measures an acoustic impedance contrast, the GPR wavefield response of the medium is determined by contrasts in electric permittivity and conductivity (Everett, 2013). GPR is governed by Maxwell's equations, often with the simplification that the magnetic permeability is spatially constant, such that the radar velocity, reflectivity, and attenuation are controlled by spatial variations in electric permittivity and conductivity. As in seismic methods, attenuation plays a large role, especially at high frequencies. In a very conductive environment such as those containing clays or saline waters, attenuation is high (Everett, 2013; Milsom and Eriksen, 2011). However, these materials are not present in significant amounts at the MMWMA field site, so GPR attenuation is modest.

3.1. Fracture Characterization

GPR is a useful technique for mapping subsurface geological structure at high spatial resolution relative to seismic data (Annan, 2009; Cassidy, 2009; Cassidy and Jol, 2009; Everett, 2013). When a dipole antenna radiates an electromagnetic wave, its

dominant polarization is parallel to the long axis of the antenna. Polarization is specified by the instantaneous direction of the electric field vector. A dipole receiver antenna similarly records the component of electric field that is oriented parallel to its long axis. A conventional bistatic system is one in which both the transmitter and receiver long axes are oriented in the same direction and maintained at fixed offset and moved along a single measurement profile (Sassen and Everett, 2009; Zeng et al., 2015). However, a traditional single-polarization survey of this type is generally insufficient to determine fracture locations and orientations; hence a multi-azimuth and/or multi-polarization approach should be considered (Seol et al., 2001; Tsoflias et al., 2004). There are four possible antennae combinations: PP, TT, TP, PT (Figure 11). There have been various multi-polarization studies using GPR to identify vertical fractures and their orientations (Sassen and Everett, 2009; Tsoflias et al., 2004)

Various conditions must be met in order to image fractures using GPR. Requirements include the existence of a significant contrast in the EM properties (mainly dielectric constant, and to a lesser extent electrical conductivity) between the rock and the fracture, taking into account both the size and fill material of the fracture (Sassen and Everett, 2009; Seol et al., 2001). The GPR frequency and polarization of the antennas should also be selected to optimize fracture detection (Sassen and Everett, 2009). The GPR response of a fracture depends on the polarization of the GPR antennae relative to the strike/dip of the fracture surface (Mejia and Young, 2007; Sassen and Everett, 2009; Seol et al., 2001; Tsoflias et al., 2004). Seol et al. (2001) described analytically, and confirmed with fieldwork, a method to find the strike direction of

fractures using multi-polarization GPR. In the azimuthal GPR method, data are acquired as the azimuth of the line-joining transmitter and receiver antennas held at fixed offset is varied through 360° rotation about a common midpoint. The zero-azimuth case corresponds to source and receiver antennas in alignment with the predominant fracture strike direction. Thus, azimuth is the angle measured between the fracture strike and the line joining the transmitter and receiver antennas (Seol et al., 2001). Since GPR reflection energy depends on the strike and dip of the fracture, the subsurface can be investigated using three antenna configurations, or "modes": perpendicular-broadside (YY or TT mode), parallel-broadside (XX or PP mode) and cross-polarization (YX or PT mode). The response R' of a fracture, at any azimuth $\emptyset$, can be related by rotation matrices to the response R at zero azimuth:

$$\begin{bmatrix} R_{XX} & R_{XY} \\ R_{YX} & R_{YY} \end{bmatrix} = \begin{bmatrix} \cos\emptyset & -\sin\emptyset \\ \sin\emptyset & \cos\emptyset \end{bmatrix} \begin{bmatrix} R'_{XX} & R'_{XY} \\ R'_{YX} & R'_{YY} \end{bmatrix} \begin{bmatrix} \cos\emptyset & \sin\emptyset \\ -\sin\emptyset & \cos\emptyset \end{bmatrix} \quad (2)$$

Using equation 2, the elements R'_{XX}, R'_{YX}, R'_{YY} with varying dip angles can be calculated to understand how the fracture azimuth and dip affect the various antenna-mode responses (Seol et al., 2001). It is possible to further look at the reflection energy, as a function of the antenna orientation, relative to the dip and strike of the fracture. Modeling results (Figure 12) show that the amplitudes of the XX mode are larger than those of the YY mode for steeply dipping fractures, 45° and 60°, while the opposite is true for a moderate dip angle of 30° (Seol et al., 2001).

To find the strike direction of a fracture, equation 2 can be expanded as

$$\begin{bmatrix} R_{XX} & R_{XY} \\ R_{YX} & R_{YY} \end{bmatrix} = \begin{bmatrix} R'_{XX}\cos\emptyset - R'_{YX}\sin\emptyset & R'_{XY}\cos\emptyset - R'_{YX}\sin\emptyset \\ R'_{XX}\sin\emptyset + R'_{YX}\cos\emptyset & R'_{XY}\sin\emptyset + R'_{YY}\cos\emptyset \end{bmatrix} \begin{bmatrix} \cos\emptyset & \sin\emptyset \\ -\sin\emptyset & \cos\emptyset \end{bmatrix} \quad (3)$$

At zero-azimuth, R_{XY} and R_{YX} will equal zero as a result of $R'_{XY} = R'_{YX}$. After some algebra, the amplitude of R_{YX} can be simplified to

$$R_{YX} = \cos\emptyset\,[R'_{XX}\sin\emptyset + R'_{YX}\cos\emptyset] - \sin\emptyset[R'_{YX}\sin\emptyset + R'_{YY}\cos\emptyset]$$

$$= -(R'_{YY} - R'_{XX})\sin\emptyset\cos\emptyset + R'_{YX}(\cos^2\emptyset - \sin^2\emptyset) \quad (4)$$

The antennas will have a specific offset during the actual data acquisition and it is possible to obtain the fracture strike direction by taking the partial derivative with respect to $\emptyset$. The above equation solved in terms of $\emptyset$ is

$$\emptyset = \frac{1}{2}\tan^{-1}\left[\frac{-\left(\frac{1}{2}A^2 - 2B^2\right) \pm \sqrt{\left(\frac{1}{2}A^2 - 2B^2\right)^2 + 4(AB)^2}}{2AB}\right] \quad (5)$$

The quantities A and B in equation 5 are A = $R'_{YY} - R'_{XX}$ and B = R'_{YX}. Seol et al. (2001) successfully applied this equation to identify fracture orientations at a granite quarry using data at several polarizations.

Tsofilias et al. (2004) and Mejia and Young (2007) have shown how vertical fractures and their orientation can be determined from responses acquired using various antenna polarizations and configurations. Based on analytical solutions and field studies, the authors show how the fracture information can be derived. Tsoflias et al. (2004) analytically compared the variation in the phase and magnitude of the responses from two orthogonal polarizations (denoted TH and TE therein) with different rock and fracture properties (Figure 13). The TH mode is characterized by the electric field oriented perpendicular to the plane of the fracture while the TE mode is characterized by the electric field oriented parallel to the plane of the fracture (Tsoflias et al., 2004). The

modeling results indicated that the phase change between the responses associated with the two polarizations is zero at low angles of incidence but increases with the angle of incidence. There is no noticeable trend of the magnitude with increasing angle of incidence. Tsolfias et al. (2004) complemented these analytic results with field observations from Bissen Quarry, with its exposed dolomite containing surface-breaking vertical fractures. Both single midpoint and 2D multi-polarization surveys were performed over the fractured floor of the quarry. The single midpoint data showed that the TH polarization response leads in time the TE polarization response, especially at later times, due to the increasing angles of incidence relative to the fracture plane (Tsoflias et al., 2004). The 2D data however showed no evidence of fractures, which is likely due to the lack of offset on the fracture surface. The author subtracted the responses from orthogonal polarizations, such as 0°-90°, after which a phase difference became apparent. The author distinguished between the heterogeneity of the dolomite and the fracture by looking at the phase change localization along the trace. If the phase change occurs along the trace, this is diagnostic of a fracture, while a lateral phase change across several traces is attributed to heterogeneity of the dolomite (Figure 14) (Tsoflias et al., 2004). This principle was confirmed with geological field observations of the fracture in outcrop. Mejia and Young (2007) also made similar observations by comparing the responses of different polarizations and antenna orientations over a large fracture at a gypsum quarry. They found that there is a clear time delay for responses using an antenna orientation in which the electric field is aligned perpendicular to the fracture. Also, when comparing the cumulative phase vs. time, there is a noticeable

change at different antennae orientations, with phase difference between 0°-60° being the largest (Figure 15) (Mejia and Young, 2007).

Grasmueck et al. (2014) acquired high-density 3D GPR data combined with outcrop observations to better understand the geometric distribution of thin, steep fractures at the Cassis Quarry in Southern France. They developed three models to help interpret diffraction signatures that were observed in their unmigrated data (Figure 16 and Figure 17). Figure 16a is a photograph of the outcrop showing many of the high angle fractures in the region with the response of the fracture seen in a 3d time slice in Figure 16b. While Figure 16c shows the steep-fracture GPR response as a series of diffractions increasing in depth (Grasmueck et al., 2014). They found that a series of point diffractors comprises the fracture signature in the GPR data (Figure 17). The model (Figure 17) shows that as more diffractors are added, due to constructive interference, the series of point diffractors merges into a continuous line. But due to destructive interference, as the number of the point diffractors is increased, only the top and bottom diffractions are seen in their entirety (Grasmueck et al., 2014).

In 2012, I helped acquire a common offset conventional bistatic GPR survey was to identify the radar signature of the fault (Figure 18). The data were acquired along the same line as the transient electromagnetic profile of Murphy (2014). The GPR section shows a large number of point diffractions beneath stations 75-95 m, which are interpreted to be originating from within the fault zone, while the diffractions beneath station 120 m at ~60-120 ns travel time are interpreted to be caused by marble/granite

heterogeneities within the footwall. The fault interpretation from the GPR image correlates well to the mapped surface expression of the fault.

3.2. Forward Modeling

Creating a model of subsurface electromagnetic properties that is representative of the fault zone at Mason, and then evaluating the forward response of such a model, is important to help interpret the fracture signatures that appear in the GPR field data. To develop such a capability, the gprMax software was used. gprMax is an open-source forward-modeling software package that uses the finite-difference time-domain (FDTD) method to simulate electromagnetic wave propagation (Giannopoulos, 2005; Warren et al., 2015). The FDTD method allows discretization in both space and time to provide a numerical solution of the governing Maxwell's equations. A 2-D version of the Yee cell is the building block of the FDTD grid (Figure 19a) (Warren et al., 2015; Yee, 1966). The 2D version of gprMax used herein implements the TT mode only (Warren et al., 2015). The specification of absorbing boundary conditions is important to avoid reflections of the waves at the modeling-domain boundaries. Absorbing boundary conditions are thus used to simulate wave propagation as if it occurred in an unbounded space (Figure 19b). A further desired characteristic of gprMax is its ability to specify material properties such as electrical permittivity and conductivity, which allows great flexibility to modify the properties of the fault zone in order to explain radar signatures that appear in the field data.

4. DATA ACQUISITION AND PROCESSING

I conducted the research in the western part of the Llano Uplift in central Texas, across a high-angle normal fault located ~12 km north of Mason, TX (Figure 20). There is easy access to the field area due to an existing good relationship with the Texas Parks and Wildlife staff at the Mason Mountain Wildlife Management Area (MMWMA) (Figure 1). With the help of a field assistant, I made multiple field trips to MMWMA in order to acquire the ground penetrating radar data (Figure 20). The multi-polarization and multi-azimuth surveys were conducted in February and March of 2015.

4.1. Data Acquisition

We collected the multi-polarization and multi-azimuth data using a pulseEKKO Pro 200 MHz ground penetrating radar system. A total of 8 lines, each with 3 different antenna polarizations (TT, PT, PP) were acquired. Additionally, we acquired lines A, B, C, D using the azimuthal procedure with the source-receiver midpoint fixed in the center of the fault zone (Figure 21). We designed the field work based on the field work done by Tsoflias et al. (2004) and Mejia and Young (2005). We acquired each line twice to test the repeatability of the data and to remove any user or other systematic error that might have occurred. We acquired the remaining 4 lines with the TX-RX midpoint fixed on one side of the fault zone: two lines (Lines E, F) with the midpoint on the Town Mountain Granite hanging wall and two lines (Lines G,H) with the midpoint on the Hickory Sandstone footwall (Figure 21). These lines were collected to help identify electromagnetic properties of the granite and sandstone units without the complication of the fault zone (i.e. these lines determine the radar velocity of the units to use with the

migration filter). The length of the survey lines that cross the fault zone is 30 m while the length of the other lines is 15 m (Figure 21). The station spacing is 0.2 m along all profiles with the antennae separation between TX and RX kept at 0.5 m for the TT and PP orientations and 0.45 m for the TP orientation. The other acquisition parameters are listed in Table 1.

One of the many challenges encountered during the field acquisition was the presence of vegetation including mesquite trees, tall grass and Opuntia cactus as well as large cobbles and stones (Figure 22). The vegetation made it difficult to acquire more than 4 lines of GPR data in the areas off the main trail. Also, multiple field trips were required due to poor weather conditions during spring 2015.

4.2. Data Processing

We processed the data using the EKKO Project software developed by the manufacturer of the GPR equipment. The software contains various processing steps that can be applied to a dataset. For the dataset, we applied De-wow, Average Background Subtraction, Stolt Migration and Automatic Gain Control in that order (Figure 23). Due to the limited change in elevation along the survey lines, we did not apply the topographic correction.

De-wow filter was the first processing step that we applied. This is a low-cut filter that removes the unwanted low-frequency signal (wow), which is induced, in part, by the proximity of the transmitter to the receiver, while preserving the wanted high-frequency signal (Cassidy, 2009; Cassidy and Jol, 2009; Everett, 2013). For the next step in the processing workflow, we applied the Background Average Subtraction filter to the

dataset. This algorithm removed the average signal across all the traces. By applying this filter, the ground clutter is greatly attenuated, allowing for a better visualization of shallow reflectors. Figure 24 shows the results of de-wow and background subtraction steps applied to the average trace on Line A, PP-mode. Next, the Stolt migration filter was applied to the data. Stolt migration is a 2-D Fast Fourier Transform (FFT) migration algorithm that collapses the hyperbolic diffractions back to their point of origin and restores the actual orientation of dipping subhorizontal reflectors (Cassidy and Jol, 2009). The Stolt migration uses only a single radar velocity for an entire line. This is problematic for this data set that features at least three different velocities, including those of two different rock and that of the fractured fault zone (Cassidy, 2009). Also, Stolt Migration, which is based on the scalar seismic migration method, does not account for the vectorial nature of electromagnetic field. The algorithm processes each mode, whether TT, PP or TP, in the same way. We selected the best radar migration velocity that was effective in collapsing the various diffractions. The velocity of 0.09 m/ns was the best overall velocity for the lines crossing the fault.

Applying an automatic gain control (AGC) was the final step of the processing sequence. Due to the attenuation caused by the electrical conductivity of the rock units, and spherical spreading of the electromagnetic wave, less energy is returned to the surface as the electromagnetic wave probes deeper into the earth. Thus, an AGC filter is applied to enhance the weaker signals contained in later arrivals (Figure 25). The AGC applies a gain that is inversely proportional to the signal strength averaged over a specified time window. The selection of time window is important because if it is too

small, noise will be amplified along with the data. Selecting a time window that is too large will result in excessive amplification of the strong signals. The AGC filter, when carefully applied, equalizes the amplitudes of the reflected signals down the entire trace. However, in this case the relative amplitude between reflectors becomes meaningless. The AGC filter for this dataset enhanced the shallow reflectors and fractures that were otherwise difficult to see.

5. RESULTS

5.1. Field Data

The 2-D radar sections (Figures 26) are 30 m long with a 110 ns record length, which corresponds to depth ~5 m using velocity 0.09 m/ns. Figure 26 shows the step-by-step processing workflow whose result appears in Figure 23 for Line A, acquired in the PP orientation. The 2-D radar sections shown in Figure 27 are of length 15 m and time duration 110 ns, but correspond to different depths due to the different migration velocity applied to the granite (v = 0.14 m/ns) and sandstone units (v = 0.12 m/ns).

The TX-RX station spacing, the velocity of the medium, and the center frequency of the GPR system, control the resolution of image. GPR resolution can be divided into two components: vertical and horizontal (Figure 28) (Annan, 2009). The vertical, or range resolution of a signal measures the ability of an observer to distinguish its cause as two different objects. If the objects are separated by a distance that is appreciably smaller than the probing radar wavelength, the two distinct parts of the signal could merge and appear to an observer as one stronger signal (Figure 29) (Annan, 2009). The following is the equation used to calculate the vertical resolution of the GPR images,

$$\Delta r \geq \frac{v}{4*f_c} \tag{6}$$

where *v* represents the velocity of the medium, while f_c is the center frequency. The center frequency for the GPR system is 200 MHz, while the nominal velocity of the geological medium, derived from the migration, is 0.09 m/ns. Using these values, the vertical resolution is ~0.1 m.

Horizontal resolution measures the ability of an observer to discern lateral changes in the radar section caused by two closely-spaced objects at the same distance from the source (Figure 28)(Annan, 2009) . The equation for horizontal resolution is

$$\Delta l \geq \sqrt{\frac{v*r}{2*f_c}} \tag{7}$$

where *r* is the distance between the source and the object, while f_c is the center frequency and *v* represents the velocity of the medium. So, as the distance increases, it becomes more difficult to distinguish smaller objects (Annan, 2009).

Due to the complex geometrical shape of the fault zone (Figure 6) that is present at the field site, the attenuation due to electrical conductivity, and scattering due to small-scale heterogeneities, loss of return signal is high. When a GPR signal is transmitted through a geological medium, the smaller scale heterogeneities scatter it in all directions. As the signal interacts with these heterogeneities within the rock medium, the reflected EM field energy is decreased (Annan, 2009).

5.2. gprMax Modeling

I analyzed synthetic reflections from dipping fractures using the finite-difference time-domain modeling software gprMax. This software is useful in creating subsurface models that contain different materials and is able to evaluate the radar responses of these models. The 2-D modeling portion of gprMax software models only the TT mode. In all the simulations, the modeled survey direction is orthogonal to the strike of the fractures. The fractures are embedded in a nonmagnetic homogeneous host material of relative permittivity $\varepsilon_r = 4$ and conductivity $\sigma = 0.002$ S/m. The fractures are simulated as a series of rectangles, similar to the circles used by Grasmeuck et al. (2014) (Figure

17). Representing the fractures as rectangles simulates irregularities in the fracture surface. The height of each rectangle is 0.5m, while the width varies depending on the length of the total fracture. To visualize the results, a simple matlab code is run to extract and display the necessary information from the gprMax output file. Due to the limitations of the output from gprMax and free processing codes available for matlab, only an AGC filter has been applied to the simulated responses.

I created two fracture models based on preliminary interpretations of the field data. The first model comprises three fractures each with a different fill material. These models were constructed to understand the response of resistive vs. conductive fracture fill material. The results showed that the strength of the EM response depends on the type of fracture fill material. (Figure 30) The second model simulates the dominant fractures observed in PP and TT mode field data. Since the 2-D forward modeling portion of the gprMax software models only the TT mode, the response of the model would hopefully represent the main aspects of the observed Line A TT radar section (Figure 31).

6. FINDINGS AND DISCUSSIONS

6.1. Field Data

To identify fractures in the 2-D radar sections, we used a combination of gained data, both migrated and unmigrated. Grasmeuck et al. (2005) and Grasmeuck et al. (2014) showed that a fracture response could be seen in the GPR data. Grasmeuck et al. (2014) identified the fractures, before migration, as a series of diffractions along the dip of the fracture (Figure 16). In migrated data, Grasmeuck et al. (2005) found that the vertical fractures diffractions were aligned into steep fracture orientations (Figure 32) . Within the migrated data (Figure 32) the fractures appear as a crosscutting feature in the GPR section (Grasmueck et al., 2005). We took a similar approach to identify these fracture signatures within the 2-D radar sections (Figure 33). Figure 33A highlights the series of diffractions observed within the fracture zone similar to Grasmueck et al. (2014). While Figure 33B shows the migrated data with some features similar to the crosscutting plane reflections seen in Figure 32B. Figure 34 shows examples of these crosscutting features that we identified as fractures (green lines). Figures 35-38 show Lines A-D with all three polarizations including interpreted locations of the fractures in green. After identifying the fractures within the data, we saw several observations, which are explained in the following sections.

6.1.1. Fractures

The first pattern we saw was that different fractures signatures are evident in different orientations along the same survey profile (Figure 39). Figure 39 shows that in the PP orientation there are a set of 3 fractures while these are not present in the TT

orientation. The mode-dependence of the fracture response indicates that different incident electric fields (i.e. different polarizations) interact with fractures differently. Looking at data from the Line A PP-mode survey configuration (Figure 32 and Figure 39), the scattered field from the fractures must contain a strong component in the direction of the RX dipole axis, which is the same as the axis of the TX dipole. In this mode, the RX dipole axis is oriented along the direction of the profile, orthogonal to the strike of the fault. The general rule states that when the incident electrical field propagates downward, the response returned upward from the fractures must be oriented along the RX axis in order to be observed (Radzevicius and Daniels, 2000; Seol et al., 2001; Tsoflias et al., 2004). The schematic diagram in Figure 40 shows an example of a propagating electric field and the response of the target. The example shows an illustration of the polarized waves propagating into the ground, interacting with the buried target, and the scattered response (Roberts and Daniels, 1996).

There are two scenarios in which the upgoing electric field vector of the PP mode will be aligned in the direction of the RX dipole axis direction. The first is if the strike of the fracture is aligned with the direction of the data acquisition profile. If the fracture strike is so oriented, and it is also the direction of the RX dipole axis, the incident field will strongly couple with the target, whereby the induced current will flow along the strike of the fracture and almost no depolarization (i.e. change in the direction of the electric field vector upon reflection from a target) will occur (Everett, 2013; Sassen and Everett, 2005, 2009). In this case, the fracture will return a scattered electric field pointing in the same direction as the RX dipole axis(Everett, 2013; Roberts and Daniels,

1996; Sassen and Everett, 2009). Sassen and Everett (2005) observed this phenomenon when doing a GPR survey over a buried conductive pipe (Figure 41). They noticed that when TX and RX are oriented in the same direction as the fracture, there was a strong response recorded (Figure 41A) (Sassen and Everett, 2005). The second scenario occurs when the fracture strike is oriented orthogonal to the data acquisition profile. In this case, the incident field will be perpendicular to the strike of the fracture while the induced currents are forced to flow along the strike of the fracture, which will cause strong depolarization. The fracture will return a scattered field that is polarized in a direction orthogonal to the RX dipole axis (Everett, 2013; Roberts and Daniels, 1996). This scenario results in the fracture not likely to be detected by a PP-mode observer. Sassen and Everett (2005) observed a similar result when mapping a buried pipe (Figure 41B). In this case, they found that when the incident electric field is oriented perpendicular to buried pipe, depolarization occurred and no response was seen in the RX (Sassen and Everett, 2005).

The above considerations are based on an assumption that the fracture fill material is conductive. If the fracture contains resistive fill material, and is excited in the PP mode, and the fracture is oriented in the direction of the data acquisition profile (that is, perpendicular to the fault) there will be strong depolarization and the fracture would not be observed in PP mode response. But, when the fracture is oriented orthogonal to the RX dipole axis, the scattered field is not strongly depolarized and it could be detected by the RX (Everett, 2013; Roberts and Daniels, 1996). From various field observations made by others from outcrops, the strike of most of the fractures in the fault

zone coincides with the strike of the fault (Becker, 1985; Harper, 2011; Randolph, 1991; Wilson, 2001). Thus, if most of the fractures are indeed oriented perpendicular to the Line A survey profile, any fractures that are observed in the PP-mode response should contain resistive fill material. The opposite is true for the fractures observed in the TT response. These fractures must behave as if filled with conductive material in order to be detected. These results support what Sassen and Everett (2005) observed in their study of mapping the buried conductive pipe. The pipe was seen in the TT orientation but not in the PP orientation (Figure 41). In summary, the fractures we observed in the PP-mode response are resistive while fractures we observed in the TT-mode response are conductive. Since these fractures are located along the same data acquisition profile, we conclude that the fractures present in this fractured geological medium have variable fill, some conductive (for, example as clay or water-filled) while others resistive (for example, as air-filled).

The same reasoning can be applied to help understand why the fracture responses observed along Lines B and C are relatively weak. In these cases, the fractures are oriented in an oblique direction to the TX and RX dipole axes for all acquisition modes. The resultant scattered electric field is not oriented in the dominant direction of the RX dipole axis and thus the receiver records only a weak signal. This is an expected consequence of the supposition that the strike of most of the fractures coincides with strike of the fault.

6.1.2. Varying Depth of Penetration

Along all GPR profiles I saw a variable depth of electromagnetic wave penetration into the various units, including the Hickory Sandstone, the fractured zone and the Town Mountain Granite. This is an indication that the different units have characteristically different dielectric properties. The Hickory Sandstone, which has the smallest depth of penetration of ~1.5 m (the weakest reflections are observed at two-way travel-time ~25 ns), is more conductive and is of lower permittivity than the Town Mountain Granite, which is characterized by depth of penetration ~2.5 m (~ 40 ns). Another indicator that the rock properties have different dielectric properties is apparent when the average velocity value of 0.09 m/ns is applied to migrate the data. This velocity is a good fit for radar returns from the Town Mountain Granite but the returns from the Hickory Sandstone units are slightly over-migrated. When a GPR section is over-migrated, some of the diffractions become upward concave "smilies" instead of collapsing onto a point.

The interpretation that depth of electromagnetic wave penetration is depended on dielectric properties, and thereby potentially lithology is further supported by examining the depth of penetration of the data acquired on the profiles located outside the fault zone. Line G, for example, is located on the Hickory sandstone; the depth of penetration is ~ 2.5 m using best-fit migration velocity 0.12 m/ns. Line E is located on the Town Mountain Granite; the depth of penetration is ~2 m at velocity 0.14 m/ns (Figure 27). The velocities used to migrate these two lines are similar to field observations from the literature on sandstones and granites (Annan, 2009; Davis and Annan, 1989). In general,

the characteristic radar velocities are slower within the fractured zone and faster in the units away from the fractured zone.

We observed an area of width ~2 m that permits deeper depth of penetration in all the lines in all antenna orientations. This area also contains more fractures compared to other areas. Looking at this area on the aerial map and comparing with field observations, this location is correlated approximately with the center of the fault zone. According to Choi et al. (2016) and Chester et al. (2004), the fault core (Figure 6) contains a higher density of fractures since this is the location of the actual slippage of the fault and hence is the site of most of the deformation. We believe that the fault core is represented in the GPR sections as an area of deeper penetration. Randolph (1991) and Wilson (2001) found that there is low-temperature, low-pressure cataclastic deformation within the fault core, which reduces the porosity and permeability of the fault zone. With reduced porosity and permeability, the medium should respond to radar probing as a resistive material. The reduction in electrical conductivity allows the EM field to travel further into the earth by limiting the attenuation compared to that of the relatively intact rock units surrounding the fault zone.

A final observation may be made from comparing data acquired on the fault zone (Figure 35) with data acquired away from it (Figure 27). The layers in the GPR sections near the fault zone show ample signs of folding while the layers in the sections away from the fault zone show significantly less folding. This can be attributed to the supposition that before the fault slip occurred, in response to the applied tectonic stress

the rocks were folded. With increasing distance from where the slippage location, the stress on the fault reduces to the stress level of the background medium.

6.2. Forward Modeling

The first modeling scenario was designed to evaluate the EM response of fractures containing different fill materials (Figure 30). The modeling specified three fractures of the same length and dip but containing distinct fill materials. From left to right in the figure, the fractures were filled with air, clay and water. Air was assigned relative permittivity $\varepsilon_r = 1$ and conductivity $\sigma = 0$ S/m. The properties of clay and water are relative permittivity $\varepsilon_r = 10$ and conductivity $\sigma = 2.0$ S/m and $\varepsilon_r = 81$, $\sigma = 0.5$ S/m, respectively. The computed model response, after an AGC filter was applied, shows three different signal strengths. In the TT-mode, the air-filled fracture generates the lowest EM response while the clay-filled fracture generates the strongest response while the water-filled fractures generates an intermediate response. This finding supports the interpretation that, in the TT-mode, resistive bodies produce the weakest radar response while conductive bodies produce stronger responses. In terms of the fractures observed in the Line A field data, in the PP mode the fractures were argued to be resistive in nature and filled with air. The TT-mode response showed different fracture responses even along the same line as the PP-mode acquisition. In the former, the incident electric field strongly couples with the fracture, causing no depolarization to occur. Hence, the returned field is polarized in the same direction as the incident field, and consequently the RX records a strong GPR signal.

The second modeling scenario created herein combines some of the major fractures observed in the Line A PP and TT-mode responses (Figure 31). The first half of the model simulated the large fractures, including size and fill, observed in the PP mode while the second half of the model simulates the large fractures observed in the TT mode. The type of fracture fill material determines the strength of the hyperbolas (i.e. the diffractions from fractures). This finding confirmed the results from the first modeling scenario and the interpretations from the field data, namely that the fault-zone fractures contain different fill materials. The modeling results also showed that in TT mode, the air-filled fractures do not couple well with the incident field and thus generate a low returned signal strength. The more conductive fractures are observed in the TT mode while the more resistive fractures are observed in the PP mode.

7. GEOPHYSICAL WORKFLOW

The following describes a new strategy from various geophysical methods, primarily guided by previous works at Llano Uplift, to find buried faults and fractures. This geophysical workflow can help locate and characterize buried faults effectively (Figure 36). The workflow should apply to large-scale surveys and to surveys focusing on small areas. This workflow can help significantly decrease the time it takes to acquire, process and interpret that data. Due to the extensive research done by the authors, the workflows presented by them are very effective in identifying various features of the faults and fractures.

The first step is to determine what characteristic or targets you are trying to distinguish in the subsurface. For example, if you are only trying to find the location of unidentified shallow faults, an aeromagnetic survey will be the only geophysical survey needed (Grauch, 2001, 2002; Howell, 2010). However, if the goal is to find specific information of the fractures located near and at a fault zone, higher resolutions surveys, such as GPR and EM surveys, are needed. The later can reveal useful information such as hydrological flows in the area (Randolph, 1991).

The second step is to understand the geologic history to gain an idea on how to design your surveys. Due to the non-unique nature of the responses of the various geophysical techniques, it is important to match geophysical results with the existing geological research in the area. The next step to the geophysical workflow is to design and execute an aeromagnetic survey. Grauch (2001, 2002) and Howell (2010) have effectively used high-resolution aeromagnetic surveys to map buried shallow faults by

studying the magnetic anomalies that are produced. In his study, Grauch (2001) ran the first aeromagnetic survey over the Albuquerque basin, New Mexico. The author acquired a series of high-resolution surveys (with a line spacing of 100-150 m) over a span of three years. Figure 37 shows the results of the surveys. After processing the data, the fault responses are seen as reliefs on aeromagnetic data. The dashed and solid lines are faults mapped or inferred from geological studies while the pink lines are concealed faults inferred from the data (Figure 37). The study concluded that various fault features (as shown by modeling of magnetic profiles) could result in these anomalies, which agrees with results of Howell (2010) (Figure 38). This illustrates how understanding the geology can help construct an accurate geological model.

Following the initial detection through aeromagnetic surveys, more detailed information about the faults can be obtained by conducting a 3-D Geometric-G858 Cesium vapor magnetometer survey (Pereira, 2013). To locate the normal fault in Mason, Texas, Pereira (2013) acquired a high-resolution 3-D magnetic anomaly profile that gave a more accurate location. These type of surveys use line spacing much denser than those of aeromagnetic surveys (~10 m instead of the ~150 m line spacing). Also, the author found that Euler deconvolution applied to reduction to pole filtered data best imaged the geological and structural contacts (Figure 9).

In the next stage of the workflow, a researcher determines what information of the fault zone is needed. If the goal is to find the location and electromagnetic properties of fractured fault zones, EM 31 or EM 34 surveys will be effective as shown by Ernstson and Kirsch (2006). Figure 39 shows the expected response of an EM 31 profile over a

fracture zone containing conductive fluids. Ernstson and Kirsch (2006) found that the apparent resistivity parallel to a set of aligned fractures was greater than the apparent resistivity measured perpendicular to the fractures (Ernstson and Kirsch, 2006). As a result knowing the tectonic stress direction, the survey can be designed such that the EM measurements are taken parallel to expected fracture orientation. In summary this type of survey can give information about the fault zone, such as its conductivity and a better estimation of the location and boundaries.

Another type of survey that can be done is the tensor controlled source time-domain electromagnetic survey conducted by Murphy (2014). He showed that by understanding the type of EM decay at different late-time responses at various TX-RX offsets could help distinguish if the fractures are conductive or resistive. At the fractured zone of the normal fault in Mason, Texas, he found that there is a faster late-time decay than $t^{-5/2}$ at long TX-RX offsets, indicating highly resistive fractures (Figure 10).

If you are trying to find the orientation and type of fractures present, a multi-polarization multi-azimuthal survey done in this research will be very effective. The multi-azimuthal survey will help identify the dominant strike of the fractures while the multi-polarization survey will help identify what type of fracture fills are present.

If this geophysical workflow is followed, the user will be able to accurately map a large unknown area of 100s of meters scale to understanding the fractures in a fractured fault zone to a cm scale. The aeromagnetic survey will help find shallow buried faults while the 3-D map will have a higher resolution. The EM 31/34 and tensor EM surveys can help identify if the fracture zone is conductive or resistive. To understand

the spatial variation of the fractures and fracture properties in the fracture zones the multi-azimuth and multi-polarization survey can be used.

8. CONCLUSIONS

The multi-polarization and multi-azimuthal acquisition at a high angle normal fault near Mason, Texas has been very successful in helping understanding the complexities of fracture zone of the fault. The following are the main conclusions of the project:

1. Multi-polarization acquisition of GPR data proved to be effective in distinguishing different fracture fills within the fault zone. There was a variation of fractures present in different orientation as seen in Line A. With the current orientations of the fractures in the fault zone, the PP orientation was able to see the resistive fractures while the TT orientation was able to record the conductive fracture fills. While the multi-azimuthal survey helped confirm that the dominant fractures in this fault zone are oriented parallel to the strike of the fault.
2. The data supported and expanded the existing knowledge of the fracture zone of the high-angle normal faults in the Llano Uplift. The 2-D radar sections showed a significant spatial variation of fracture orientations and size compared to the results seen by researchers in outcrop.
3. The effect of the fault on the nearby rock units can be seen when comparing the survey lines from on the fault to nearby the fault. The velocity of the layers near the fault zone is less (v = 0.09 m/ns) than the velocity of the individual units away from the fault zone (v = 0.12 m/ns for Hickory Sandstone and 0.14 m/ns for Town Mountain Granite). Lower velocity values indicate a higher dielectric constant while the higher velocity values indicate a lower dielectric constant. The

lower velocity can be attributed to the increased amount of fractures within the fault zone that are causing the radar waves to slow down.

4. gprMax 2-D forward modeling software confirmed the results seen in the multi-polarization data. In the TT orientation, when the fractures are perpendicular to the survey profile, the conductive fractures will have a stronger signal compared to the resistive fractures.
5. A comprehensive geophysical workflow has been proposed that will be effective in mapping shallow unseen faults and derive various characteristics about the fractures and the fault zone in a new field area.

9. SUMMARY AND IMPLICATIONS

Application of multi-azimuth and multi-polarization ground penetrating radar has allowed the fractured fault zone of a Pennsylvanian high-angle normal fault in Mason County to be characterized accurately. The results from the research show that in a multi-polarization acquisition, it is easier to distinguish different properties of the fractures present. When comparing the PP survey profile with the TT profile, it was seen that there were some fractures that acted in a resistive manner while some fractures were more conductive in nature. The multi-azimuth survey helped identify the orientation of the fractures. Due to the orientation of the GPR TX and RX, it was seen that the dominant strike orientation of the fractures was parallel to the strike of the fault. This was confirmed by using gprMax modeling software. The modeling showed that in the TT orientation, the resistive fractures have significantly lower energy response than the conductive fractures. We identified conductive fractures and resistive fractures as well as the fault core within the fracture zone. Due to the strength in the GPR acquisition technique, we were able to accurately map the spatial variation in the fractures and fracture fill of the fracture zone of the high angle normal fault in the Llano Uplift.

The experience gained in this research and previous graduate students research at the Llano Uplift allowed us to create a geophysical workflow that will be efficient in identifying shallow faults and characterize the faults that do not have a surface exposure. This workflow can be used to help map faults in a new area that has not been studied. The workflow contains geophysical methods for various degree of exploration, from surveying 100's of meters by using aeromagnetic surveys to densely gridded surveys

(meter scale) GPR surveys. The results from the study have direct implications for future fieldwork in characterizing fault zones in other areas in a quick and timely manner.

REFERENCES

Amsbury, D., and W. Haenggi, 1993, Middle Pennsylvanian strike-slip faulting in the Llano Uplift, central Texas, Bulletin Houston Geological Society.

Annan, A., 2009, Electromagnetic principles of ground penetrating radar, v. 1, chapter.

Becker, J. E., 1985, Structural analysis of the western Llano uplift with emphasis on the Mason fault, Texas A&M University.

Cassidy, N. J., 2009, Electrical and magnetic properties of rocks, soils and fluids: Ground Penetrating Radar Theory and Applications, p. 41-72.

Cassidy, N. J., and H. Jol, 2009, Ground penetrating radar data processing, modelling and analysis: Ground Penetrating Radar Theory and Applications, p. 141-176.

Chester, F., J. Chester, D. Kirschner, S. Schulz, and J. Evans, 2004, Structure of large-displacement, strike-slip fault zones in the brittle continental crust: Rheology and Deformation in the Lithosphere at Continental Margins, v. 1, p. 223-260.

Chester, F. M., J. P. Evans, and R. L. Biegel, 1993, Internal structure and weakening mechanisms of the San Andreas fault: Journal of Geophysical Research: Solid Earth, v. 98, p. 771-786.

Choi, J.-H., P. Edwards, K. Ko, and Y.-S. Kim, 2016, Definition and classification of fault damage zones: A review and a new methodological approach: Earth-Science Reviews, v. 152, p. 70-87.

Cohrs, F. J. R., 2012, Seismoelectric Imaging of a Shallow Fault System Employing Fault Guided Waves, Texas A&M University.

Dalziel, I. W., S. Mosher, and L. M. Gahagan, 2000, Laurentia-Kalahari collision and the assembly of Rodinia: The Journal of Geology, v. 108, p. 499-513.

Davis, J., and A. Annan, 1989, Ground-penetrating radar for high-resolution mapping of soil and rock stratigraphy1: Geophysical prospecting, v. 37, p. 531-551.

Ernstson, K., and R. Kirsch, 2006, Aquifer structures: fracture zones and caves, Groundwater Geophysics, Springer, p. 395-422.

Everett, M. E., 2013, Near-surface applied geophysics, Cambridge University Press.

Faulkner, D., A. Lewis, and E. Rutter, 2003, On the internal structure and mechanics of large strike-slip fault zones: field observations of the Carboneras fault in southeastern Spain: Tectonophysics, v. 367, p. 235-251.

Garrison, J. R., and D. Mohr, 1983, Geology of the Precambrian Rocks of the Llano Uplift, Central Texas: Field Trip Notes: Field Trip Notes for 1983 Geological Society of America South-Central Section Field Trip--central Mineral Region Crystalline Rocks, Llano Uplift, Central Texas, March 5-6, 1983, College of Geosciences, Texas A & M University.

Giannopoulos, A., 2005, Modelling ground penetrating radar by GprMax: Construction and building materials, v. 19, p. 755-762.

Grasmueck, M., T. J. Moser, M. A. Pelissier, J. Pajchel, and K. Pomar, 2014, Diffraction signatures of fracture intersections: Interpretation, v. 3, p. SF55-SF68.

Grasmueck, M., R. Weger, and H. Horstmeyer, 2005, Full-resolution 3D GPR imaging: Geophysics, v. 70, p. K12-K19.

Grauch, V., 2001, High-resolution aeromagnetic data, a new tool for mapping intrabasinal faults: Example from the Albuquerque basin, New Mexico: Geology, v. 29, p. 367-370.

Grauch, V., 2002, High-resolution aeromagnetic survey to image shallow faults, Dixie Valley geothermal field, Nevada, US Department of the Interior, US Geological Survey.

Harper, R. A., 2011, Geology of the McMillan Ranch in Mason, Texas: An Assessment of the Nature of Normal Faults in the Mason Area, Texas A&M University.

Howell, L. E., 2010, Characterizing shallow intrasedimentary faults using magnetic depth estimation methods: Preliminary results of a high-resolution aeromagnetic survey at the San Luis Basin, south-central Colorado, Carleton College.

Mejia, D. R., and R. A. Young, 2007, Fracture orientation determination in sedimentary rocks using multicomponent ground-penetrating radar measurements: The Leading Edge, v. 26, p. 1010-1016.

Merrill, G. K., R. C. Grayson Jr, L. L. Lambert, and M. J. Pranter, 1991, Introduction to the Llano Uplift Region. Carboniferous geology and tectonic history of the southern Fort Worth (Foreland) basin and Concho platform, Texas, p. 1-2.

Milsom, J. J., and A. Eriksen, 2011, Field geophysics, v. 36, John Wiley & Sons.

Mosher, S., 1998, Tectonic evolution of the southern Laurentian Grenville orogenic belt: Geological Society of America Bulletin, v. 110, p. 1357-1375.

Mosher, S., J. Levine, and W. Carlson, 2008, Mesoproterozoic plate tectonics: A collisional model for the Grenville-aged orogenic belt in the Llano uplift, central Texas: Geology, v. 36, p. 55-58.

Murphy, B. C., 2014, Fault Characterization using Induced Electric Currents Presumed to Undergo Anomalous Diffusion in Mason, Texas, Texas A&M University.

Nelis, M. K., S. Mosher, and W. D. Carlson, 1989, Grenville-age orogeny in the Llano Uplift of central Texas: Deformation and metamorphism of the Rough Ridge Formation: Geological Society of America Bulletin, v. 101, p. 876-883.

Pereira, A. D. N., 2013, Geophysical Fault Mapping Using the Magnetic Method at Hickory Sandstone Aquifer, Llano Uplift, Texas, Texas A&M University.

Radzevicius, S. J., and J. J. Daniels, 2000, Ground penetrating radar polarization and scattering from cylinders: Journal of Applied Geophysics, v. 45, p. 111-125.

Randolph, L. C., 1991, The effects of faults on the groundwater system in the Hickory Sandstone Aquifer in Central Texas: Master's Thesis, Texas A&M University

Roberts, R. L., and J. J. Daniels, 1996, Analysis of GPR polarization phenomena: Journal of Environmental and Engineering Geophysics, v. 1, p. 139-157.

Sassen, D. S., and M. E. Everett, 2005, Multi-component ground penetrating radar for improved imaging and target discrimination: 18th EEGS Symposium on the Application of Geophysics to Engineering and Environmental Problems.

Sassen, D. S., and M. E. Everett, 2009, 3D polarimetric GPR coherency attributes and full-waveform inversion of transmission data for characterizing fractured rock: Geophysics, v. 74, p. J23-J34.

Seol, S. J., J.-H. Kim, Y. Song, and S.-H. Chung, 2001, Finding the strike direction of fractures using GPR: Geophysical Prospecting, v. 49, p. 300-308.

Teran, I. A., 2007, Stratal architecture and sedimentology of a portion of the Upper Cambrian Hickory Sandstone, central Texas, USA: Master's thesis, Texas A&M University.

Tsoflias, G. P., J.-P. Van Gestel, P. L. Stoffa, D. D. Blankenship, and M. Sen, 2004, Vertical fracture detection by exploiting the polarization properties of ground-penetrating radar signals: Geophysics, v. 69, p. 803-810.

Warren, C., A. Giannopoulos, and I. Giannakis, 2015, An advanced GPR modelling framework: The next generation of gprMax: Advanced Ground Penetrating Radar (IWAGPR), 2015 8th International Workshop on, p. 1-4.

Weiss, C. J., and M. E. Everett, 2007, Anomalous diffusion of electromagnetic eddy currents in geological formations: Journal of Geophysical Research: Solid Earth, v. 112.

Wilson, J. S., 2001, High-resolution stratigraphic and structural characterization of the fault-partitioned Hickory Sandstone aquifer system, Mason County, central Texas: Master's Thesis thesis, Texas A&M University.

Yee, K. S., 1966, Numerical solution of initial boundary value problems involving Maxwell's equations in isotropic media: IEEE Trans. Antennas Propag, v. 14, p. 302-307.

Zeng, Z., Z. Zhaofa, L. Jing, H. Ling, F. Xuan, and L. Fengshan, 2015, Improving Target Detection Accuracy Based on Multipolarization MIMO GPR: IEEE Transactions on Geoscience and Remote Sensing, v. 53, p. 15-24.

APPENDIX

FIGURES

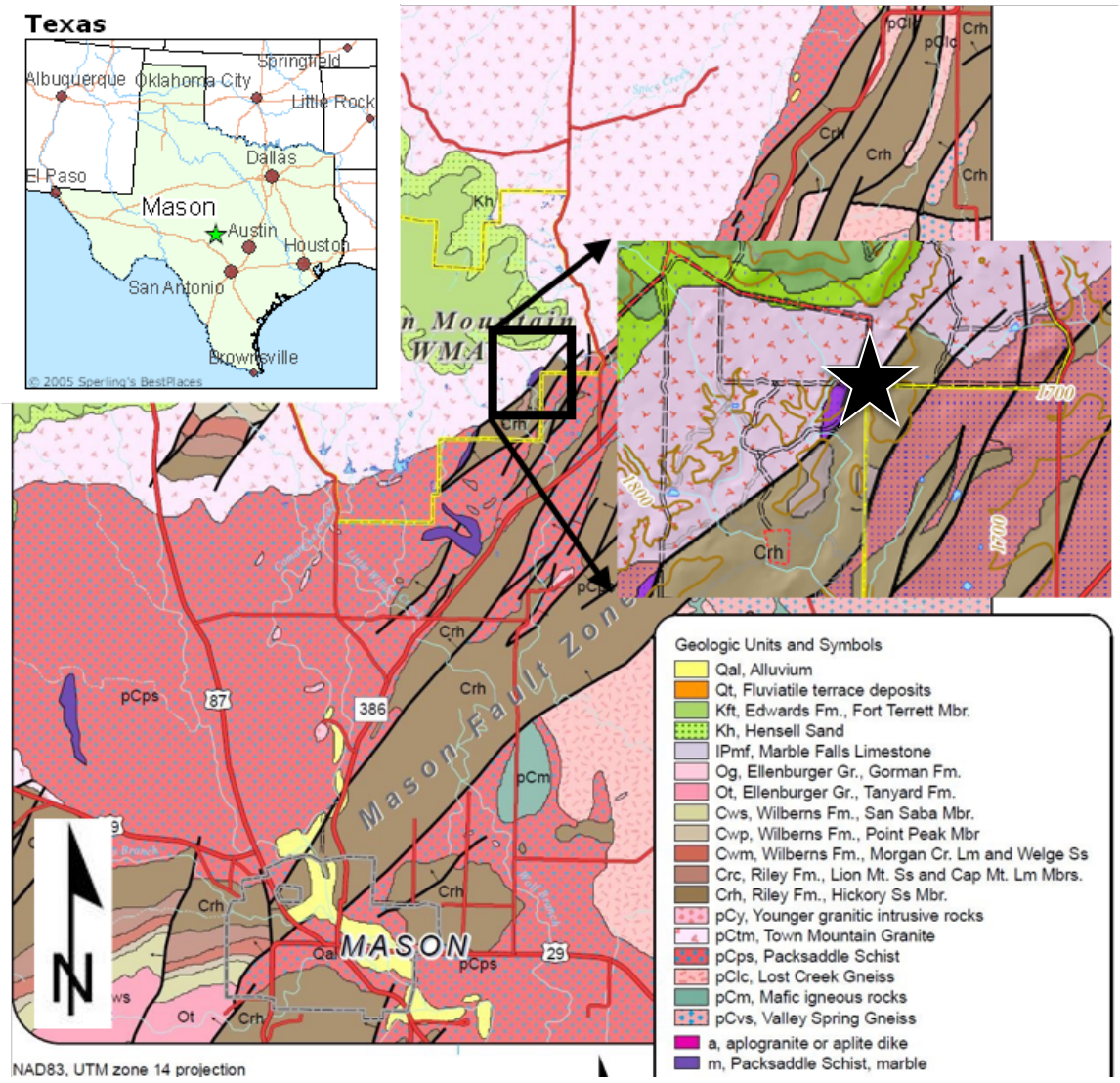

Figure 1: Geologic map Mason with the study area boxed in black. The black star shows the approximate location of the survey. The green star on the inset shows the location of Mason, TX [modified from *M Helper, 2006*].

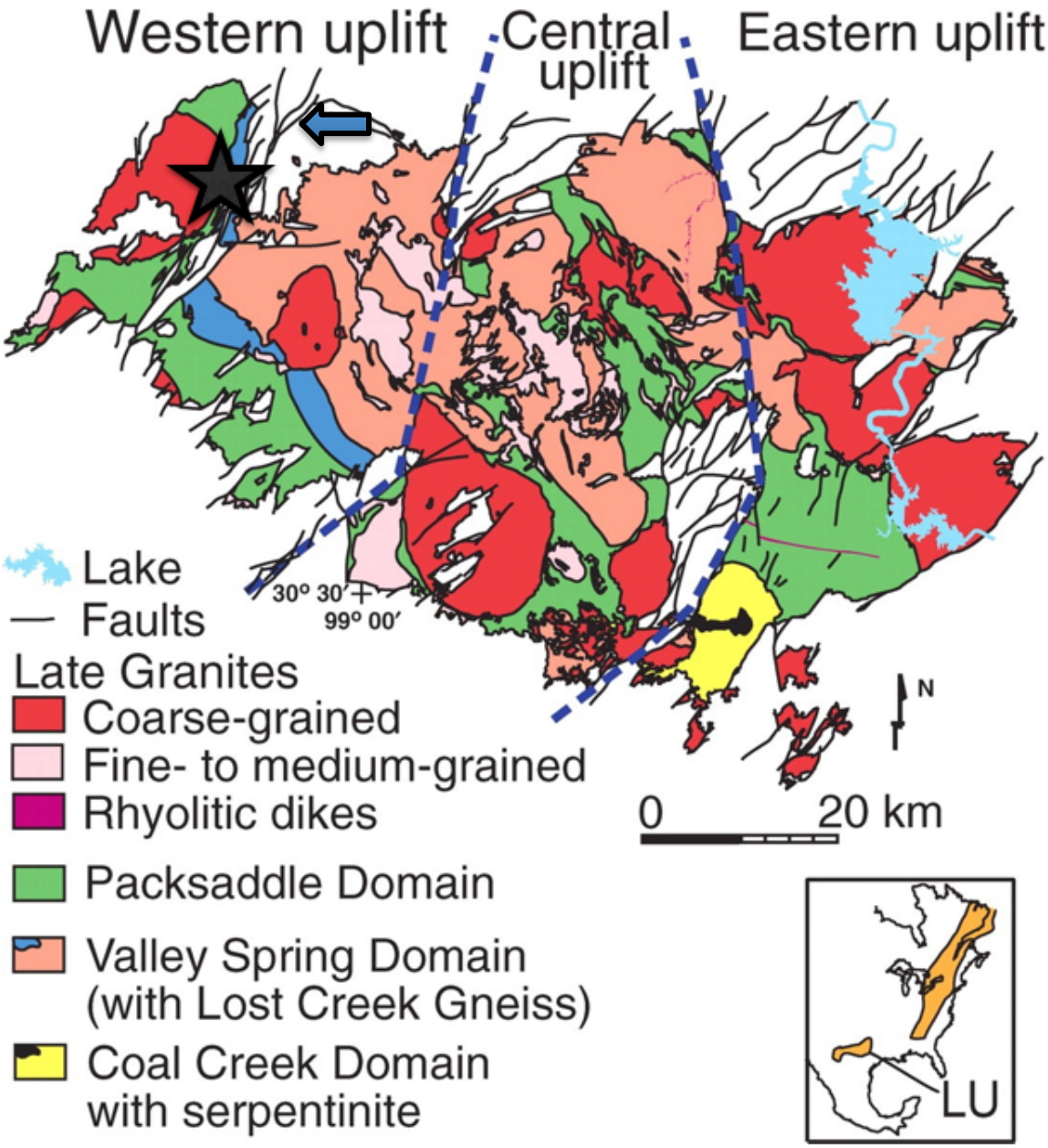

Figure 2: Geologic map of the Llano Uplift showing major fault trends. The black star represents the approximate location of the research area. The blue arrow is pointing to the high angle normal faults seen in the area (modified from Mosher et al., 2008).

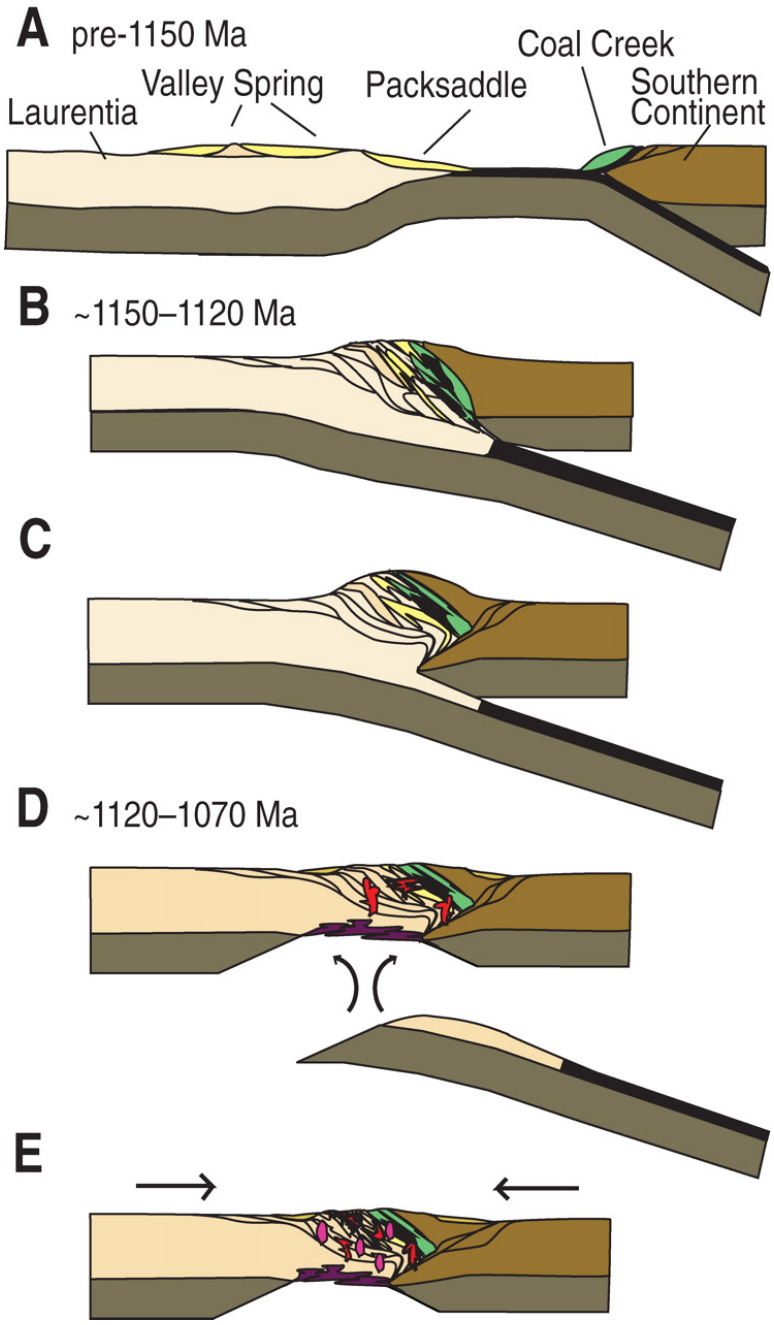

Figure 3: Tectonic model of the formation of the Llano Uplift caused by the formation of Rodinia. A-E demonstrates from the continent-continent collision to the formation of the strike slip fault systems (Mosher et al., 2008).

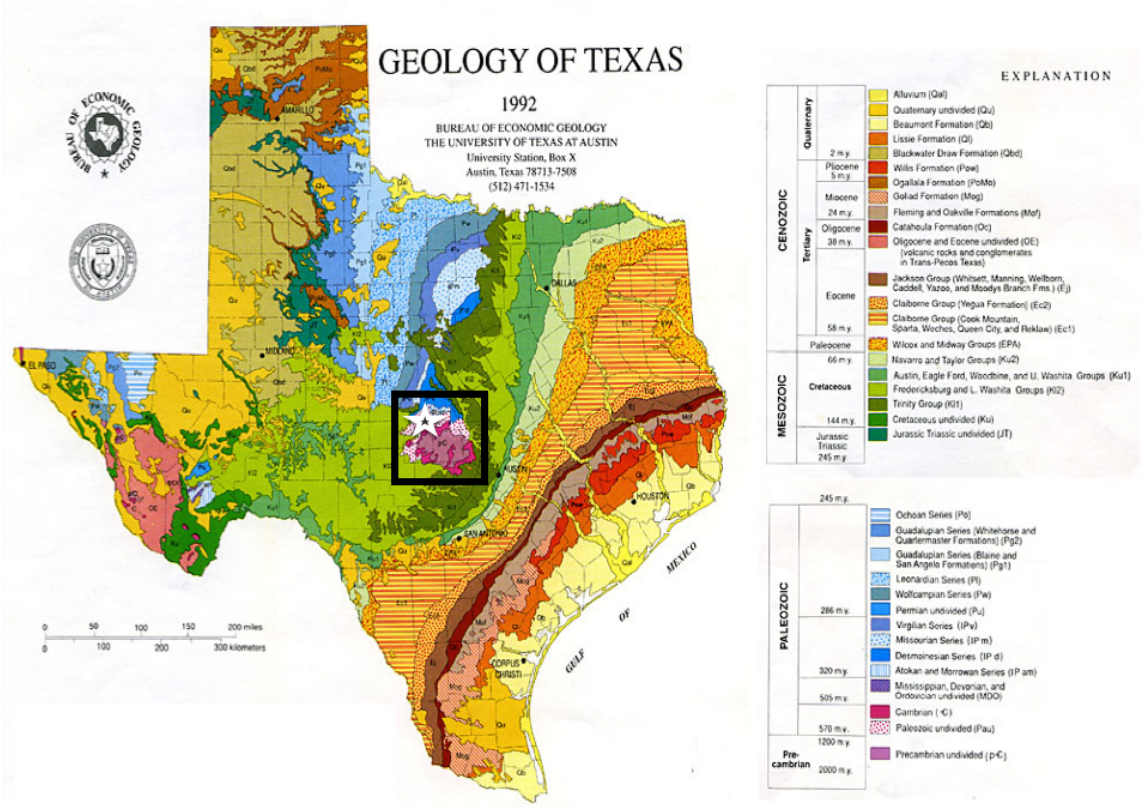

Figure 4: Geologic map of Texas. The black box is showing the Pre-Cambrian extrusion caused by Llano Uplift. The white star is the approximate location of the field site (Bureau of Economic Geology, 1992).

Era	System	Group	Formation	Member or unit
Paleozoic	Ordovician	Ellenberger Group	Honeycut Formation	Undivided
			Gorman Formation	Undivided
			Tanyard Formation	Staendebach Member
				Threadgill Member
	Medium to upper Cambrian	Moore Hollow Group	Wilberns Formation	San Saba Member
				Point Peak Member
				Morgan Creek Limestone Member
				Weldge Sandstone Member
			Riley Formation	Lion Mountain Sandstone Member
				Cap Mountain Limestone Member
				Hickory Sandstone Member
Precambrian	Valley Spring Gneiss/Packsaddle Schist/Town Mountain Granite			

Subunits
Upper Hickory
Medium Hickory
Lower Hickory

Figure 5: Stratigraphic column showing the rock units of importance for the field area in orange. Image modified from (modified from Teran, 2007).

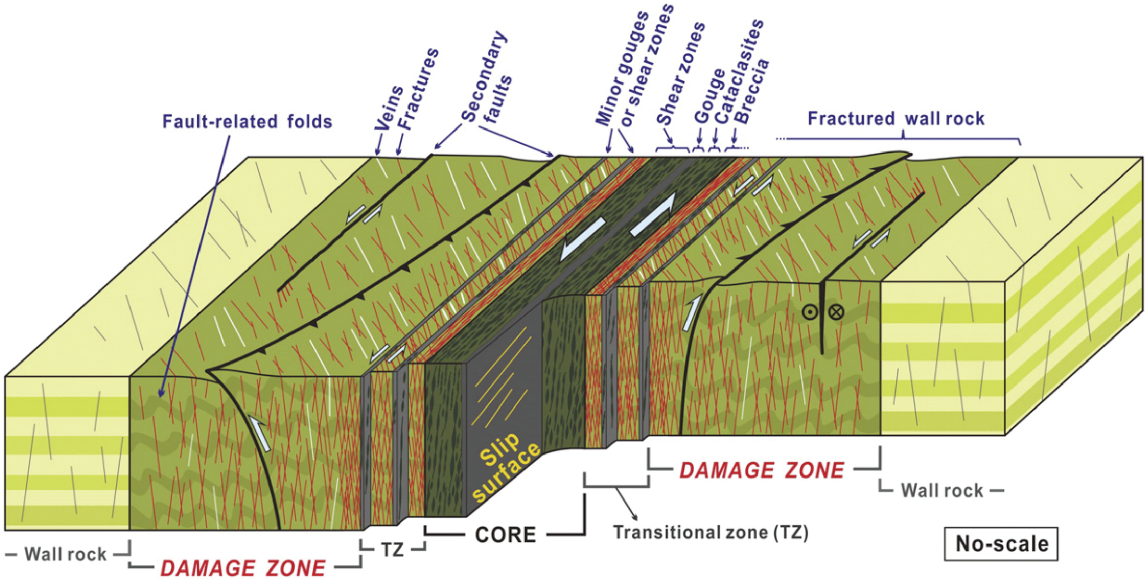

Figure 6: Cartoon diagram showing the various components of a fault zone of a strike slip fault (Choi et al., 2016).

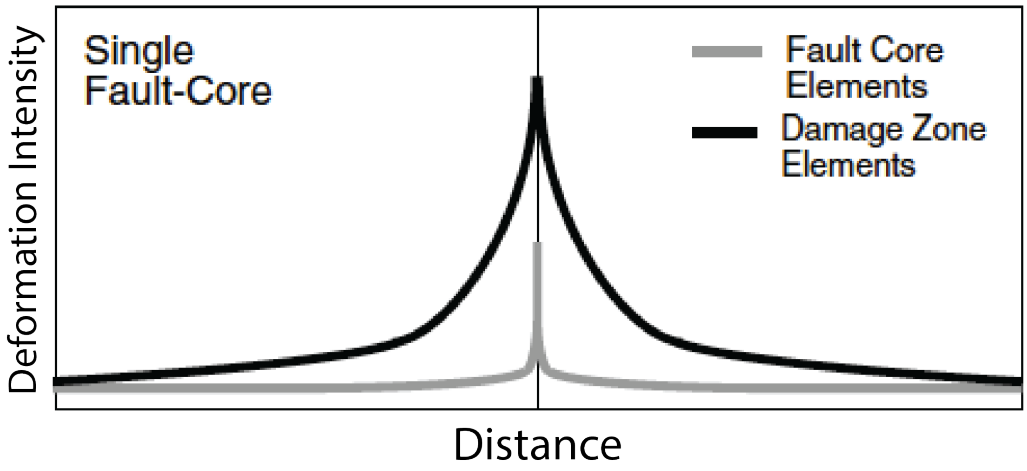

Figure 7: A figure displaying the expected deformation intensity of a fault zone from the fault core. The deformation intensity (fractures) decreases from the fault core to the end of the damage zone modified from (modified from Chester et al., 2004).

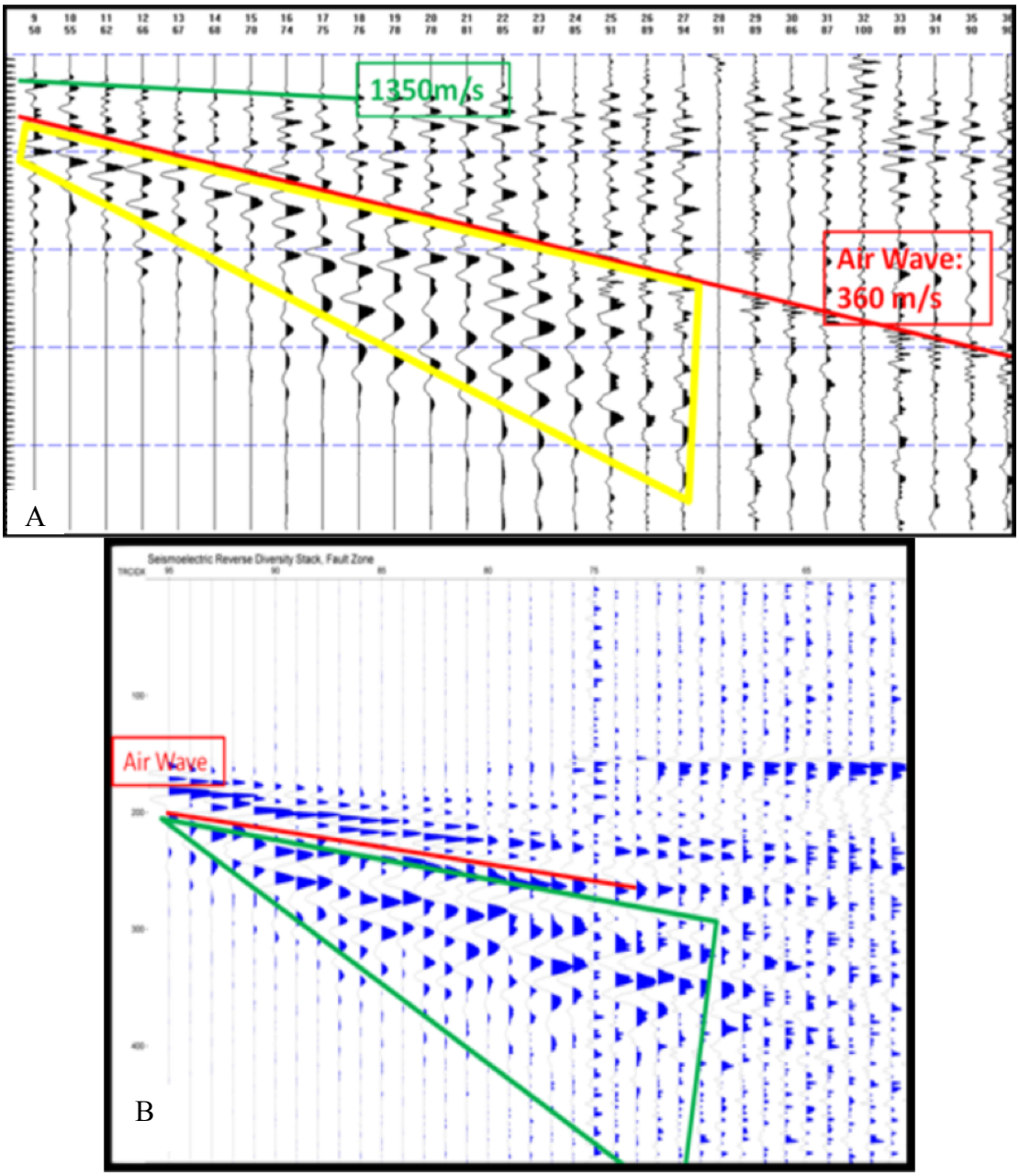

Figure 8: Part A is the seismic record while Part B is the seismoelectric surveys. The yellow and the green quadrilaterals show the late arriving fault-guided waves. (Cohrs, 2012)

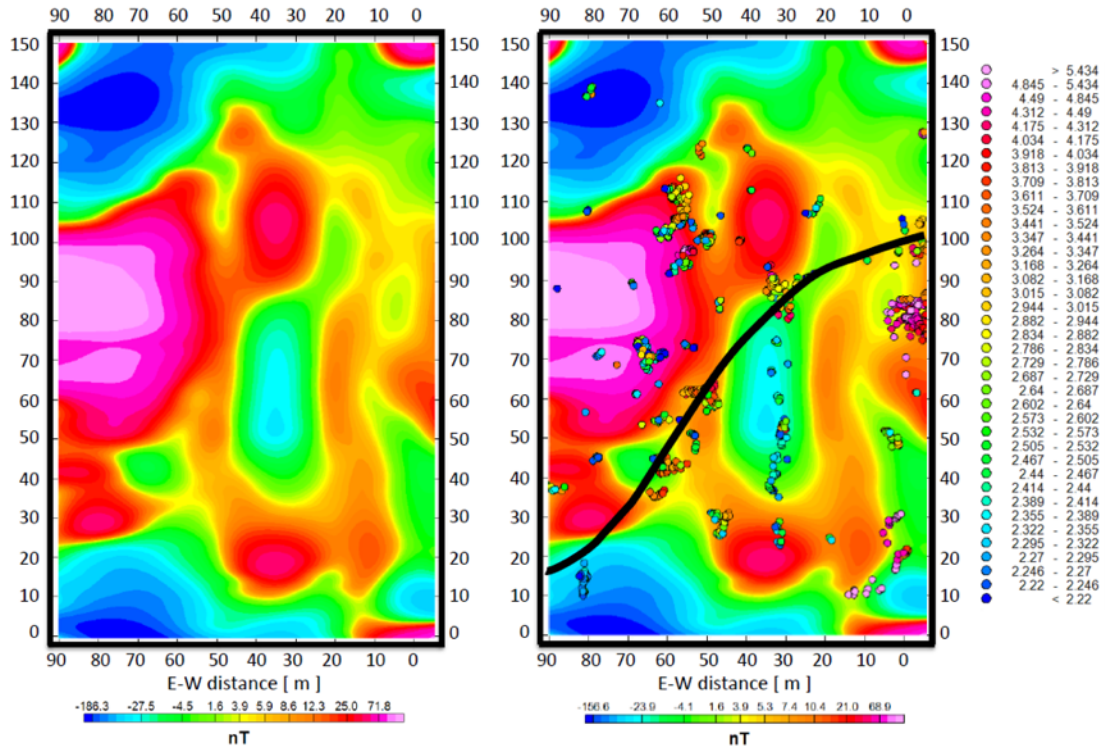

Figure 9: (left) The magnetic gradient map of the survey area after reduction-to-pole filtering and (right) with Euler deconvolution with the fault interpretation in black. (Pereira, 2013)

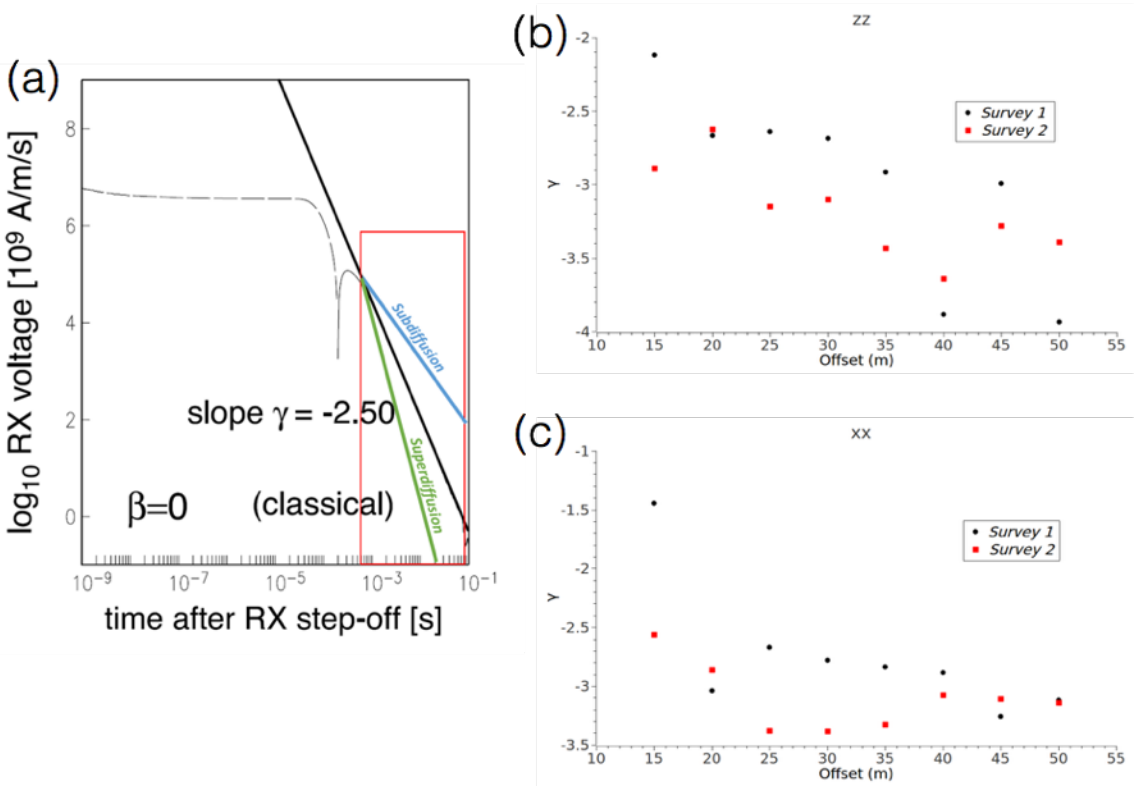

Figure 10: (a) Theoretical log-log plot of the EM response. The red box is the decay of the EM response as seen in b and c. (b, c) both show a late-time slope that is decreasing with increasing offset. This indicates increase in roughness of the medium, which suggests highly resistive fractures in the fault zone. (modified from Murphy, 2014)

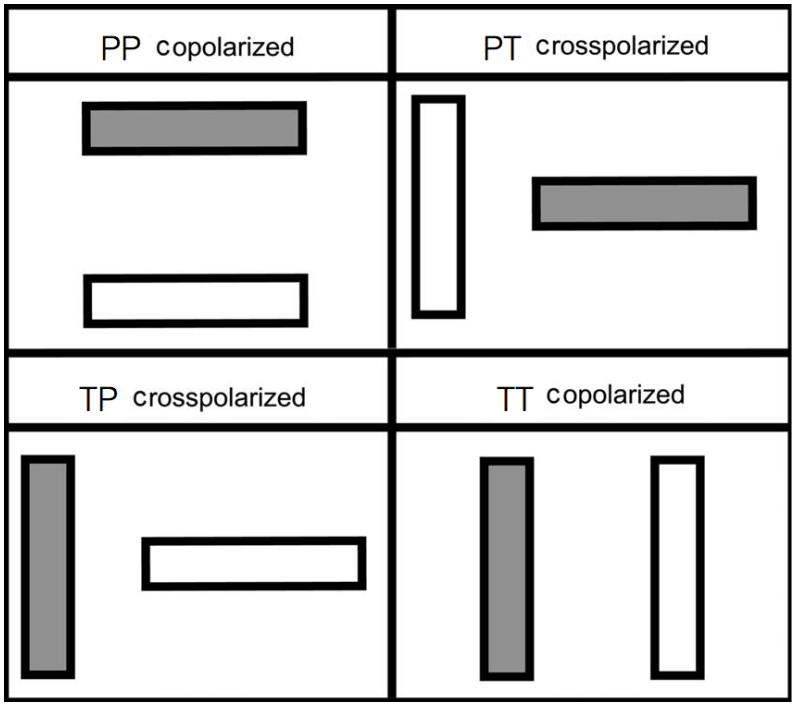

Figure 11: Various antennae orientations with the grey block representing the transmitting antenna and the white representing the receiving antenna. The transmitter and the receiver are moving to the right. (modified from Sassen and Everett, 2009).

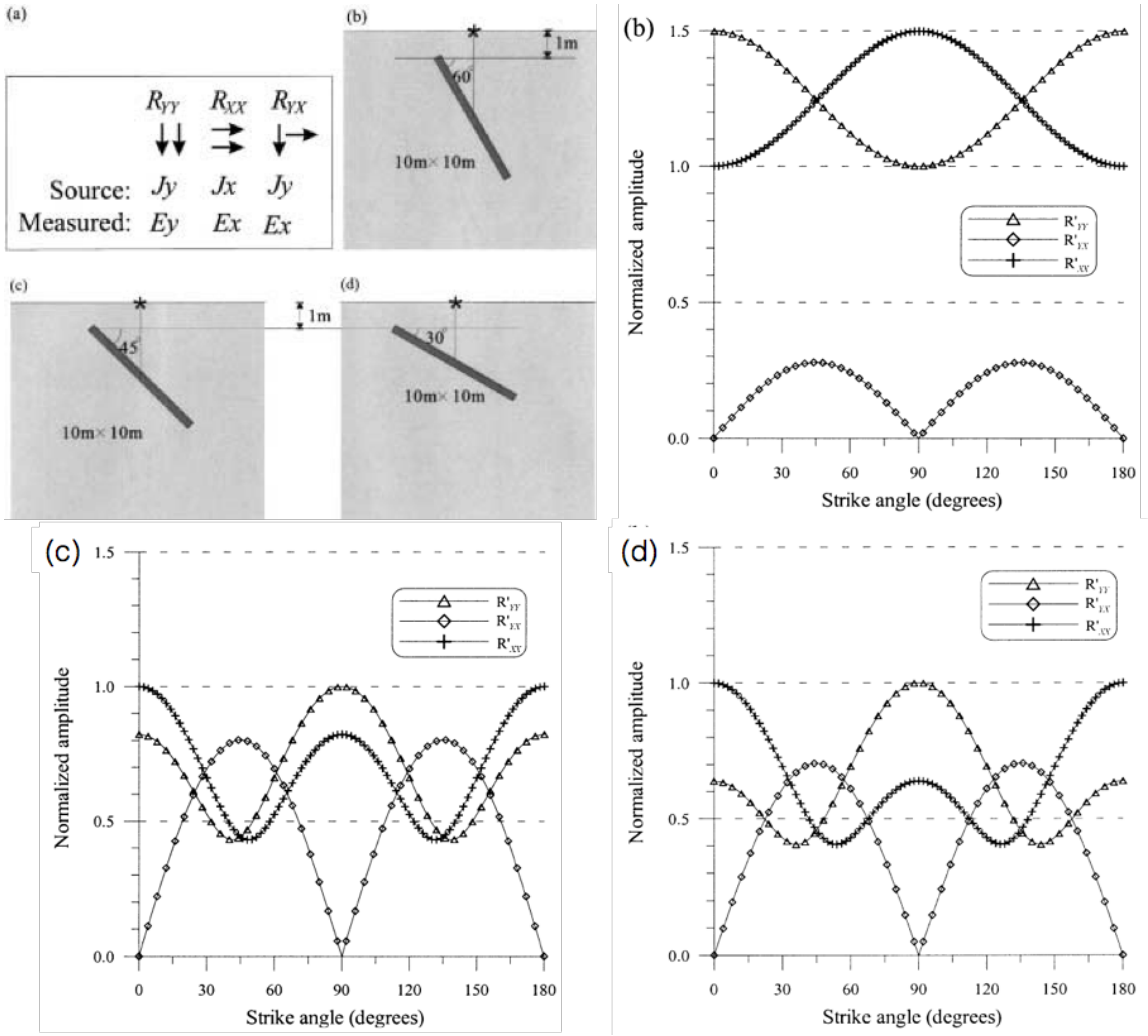

Figure 12: a) Schematic of the different polarizations; Cross-section view with the dipping sheet (black rectangle) representing fault with varying dipping angle. (b) 30°,(c) 45°, (d) 60°. The amplitude plots (b,c,d) show that the XX mode is larger than YY for a steeply dipping fracture, 45° and 60°, while the opposite is true for dip angle of 30°. (modified from Seol et al., 2001).

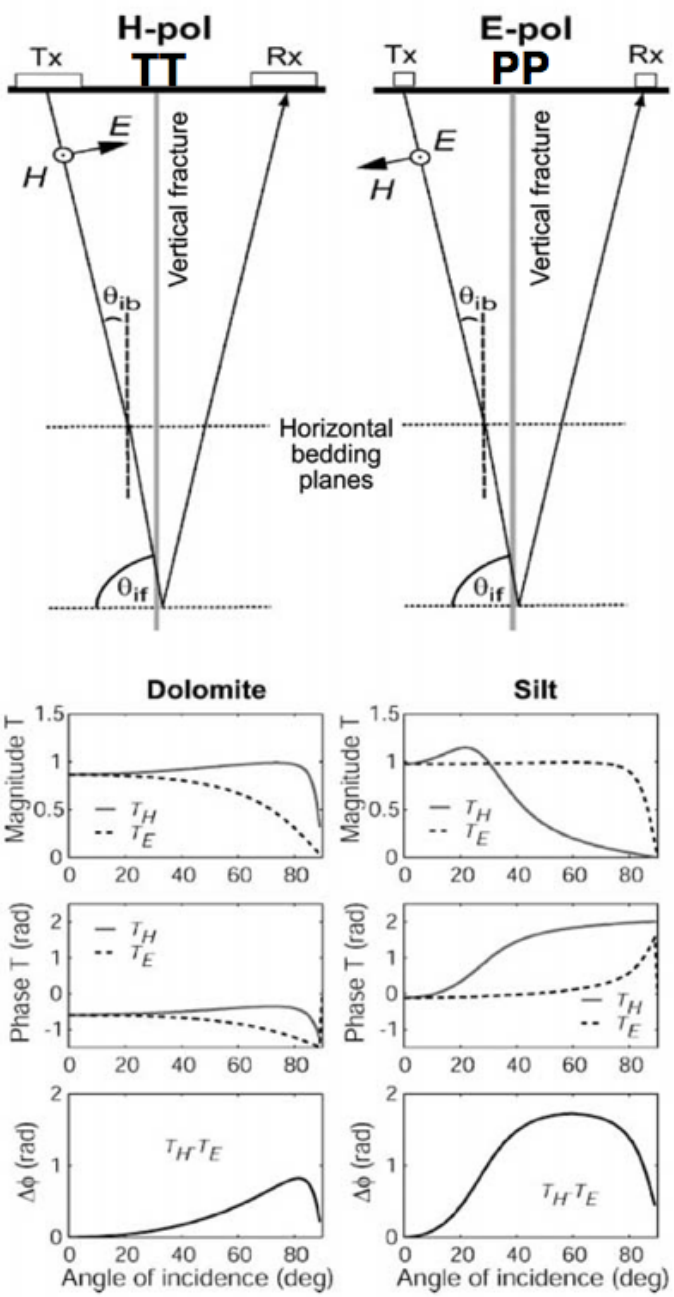

Figure 13: Simplified electromagnetic wavefield geometry. The figures in the bottom are the solutions that are showing the magnitude, phase and the phase difference of the Dolomite rock matrix with water saturated fracture and silt rock matrix containing air filled fracture. (modified from Tsoflias et al., 2004)

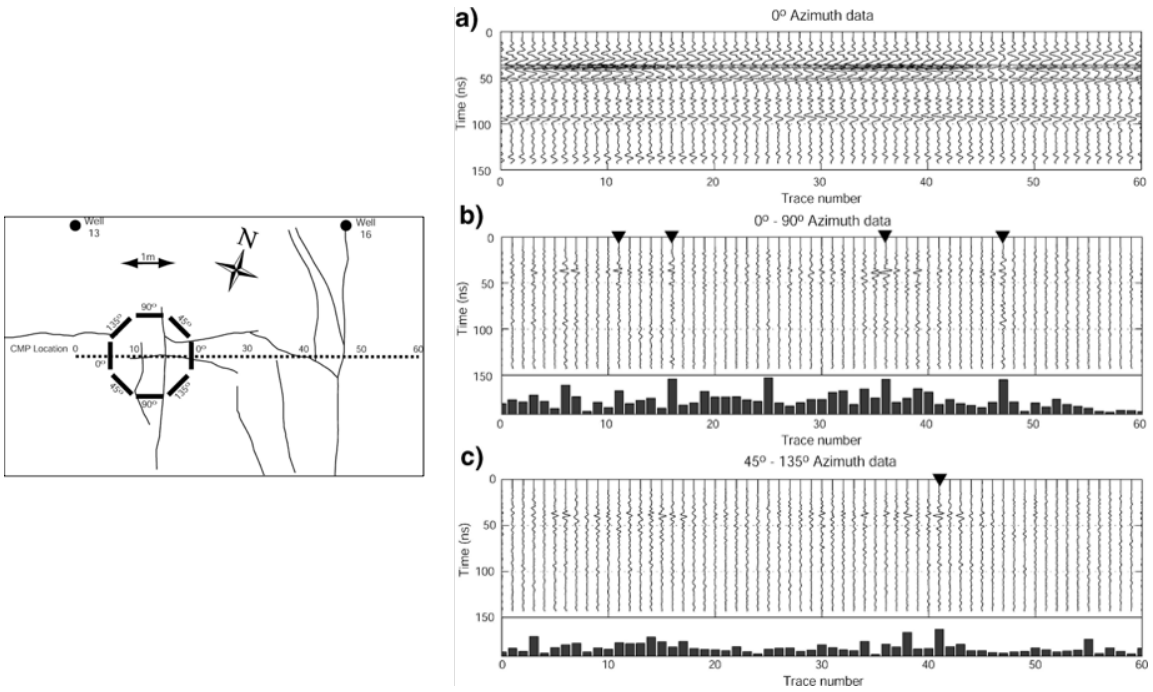

Figure 14: (Left) Geometry of the 2D multiazimuth survey. (Right) 2D multiazimuth survey data; (a) Data at zero degree azimuth; (b,c) Difference azimuth subtracted data that shows the fracture response. The black triangles represent the field observations of the vertical fracture. The bar graphs show the sum of squared amplitudes along each trace. (modified from Tsoflias et al., 2004)

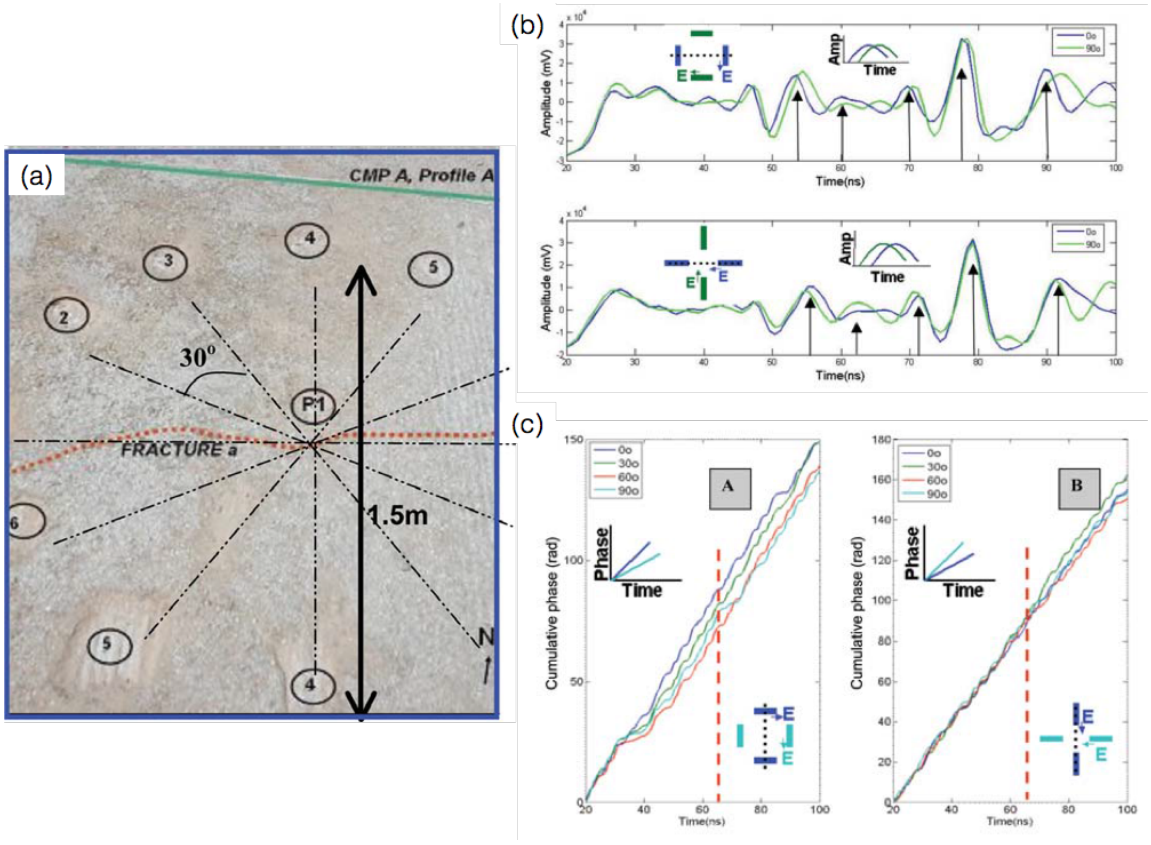

Figure 15: (a) A common midpoint survey geometry at a gypsum quarry with the fracture represented by the orange dotted line. (b) Comparison of traces with the YY configuration, the EM field is polarized perpendicular to the fracture (blue trace) and parallel to the fracture (green trace). The bottom of (b) is the XX configuration with colors representing the opposite. The arrows are pointing to when a trace is leading the other orientation. (c) Shows the cumulative phase change between different orientations (zero to ninety degrees). (modified from Mejia and Young, 2007)

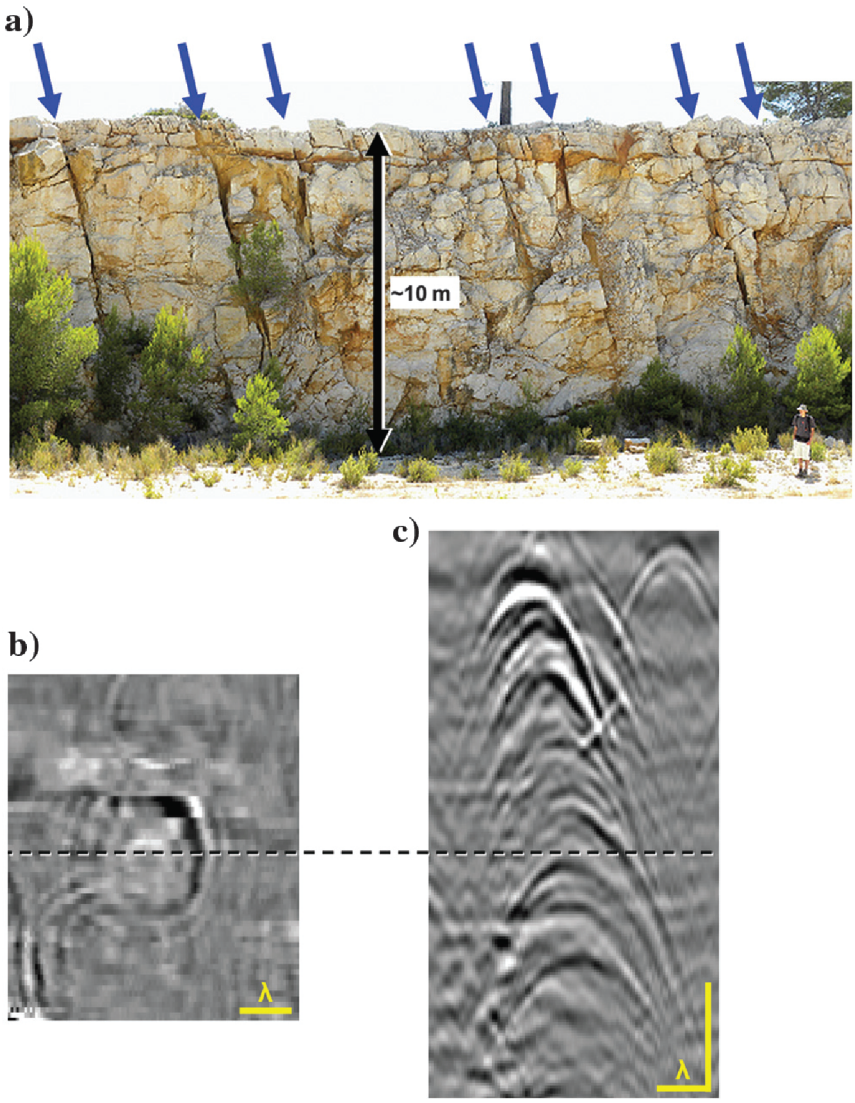

Figure 16: (a) Photograph of the outcrop with the blue arrows pointing to the various steep dipping fractures. (b) Time slice of the 3D GPR data. (c) 2D line showing the diffractions which represents one of the fractures seen in (a). (Grasmueck et al., 2014)

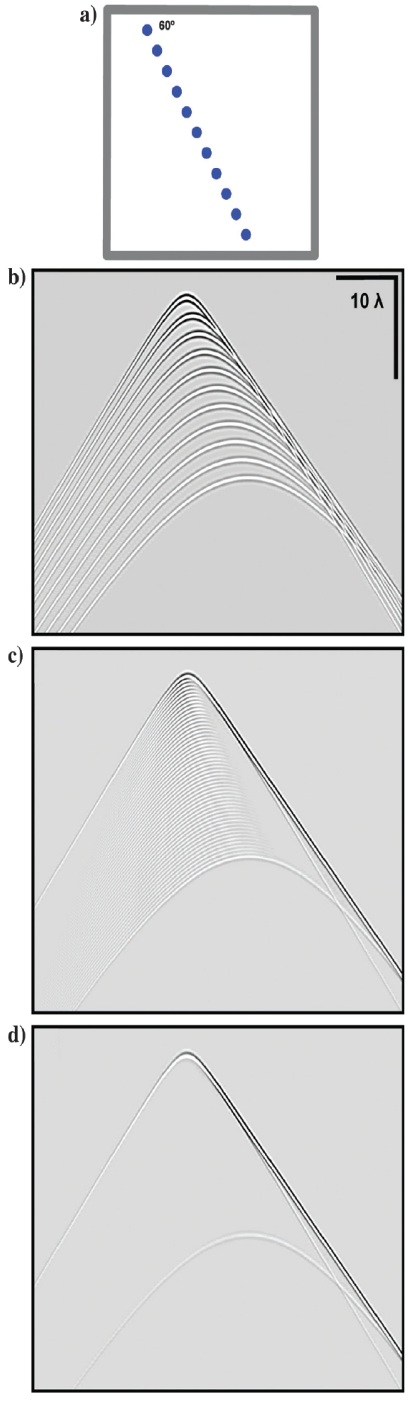

Figure 17: (a) A model with 11 point diffractors along a 60 degree slope. (b-d) Synthetic data showing the diffraction response of the point diffractors. The change from b through d is the spacing the point diffractors seen in part a. From b through d the number of points has increased as well from 11 to 101 point diffractors. (Grasmueck et al., 2014)

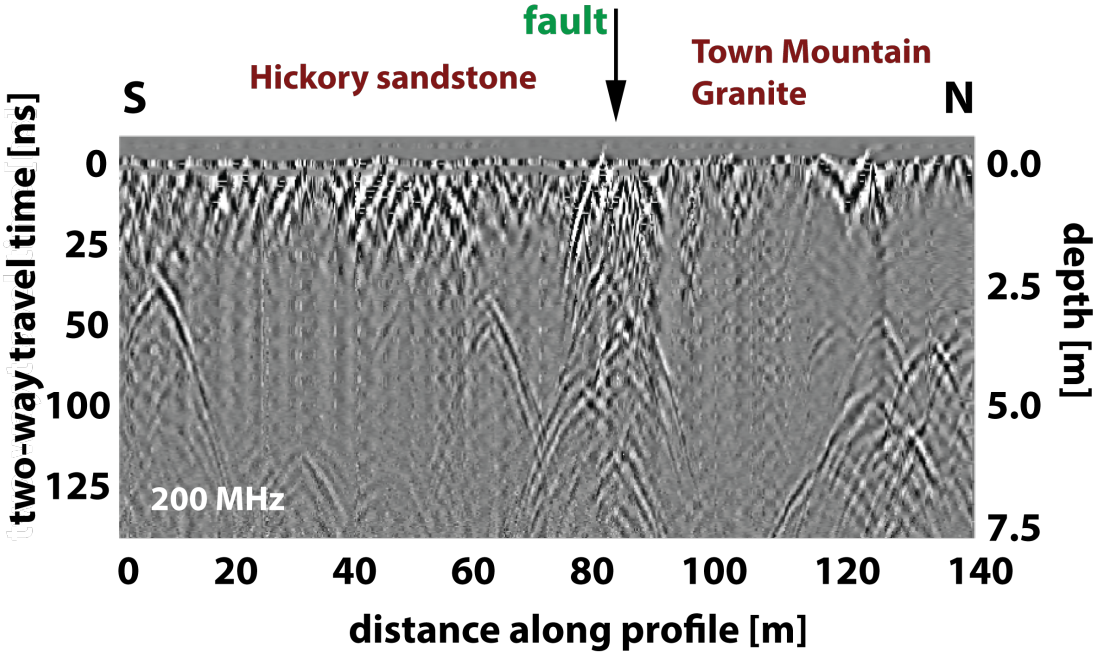

Figure 18: A common offset GPR survey across the fault. The black arrow points to the location of the high angle normal fault in Mason, Texas.

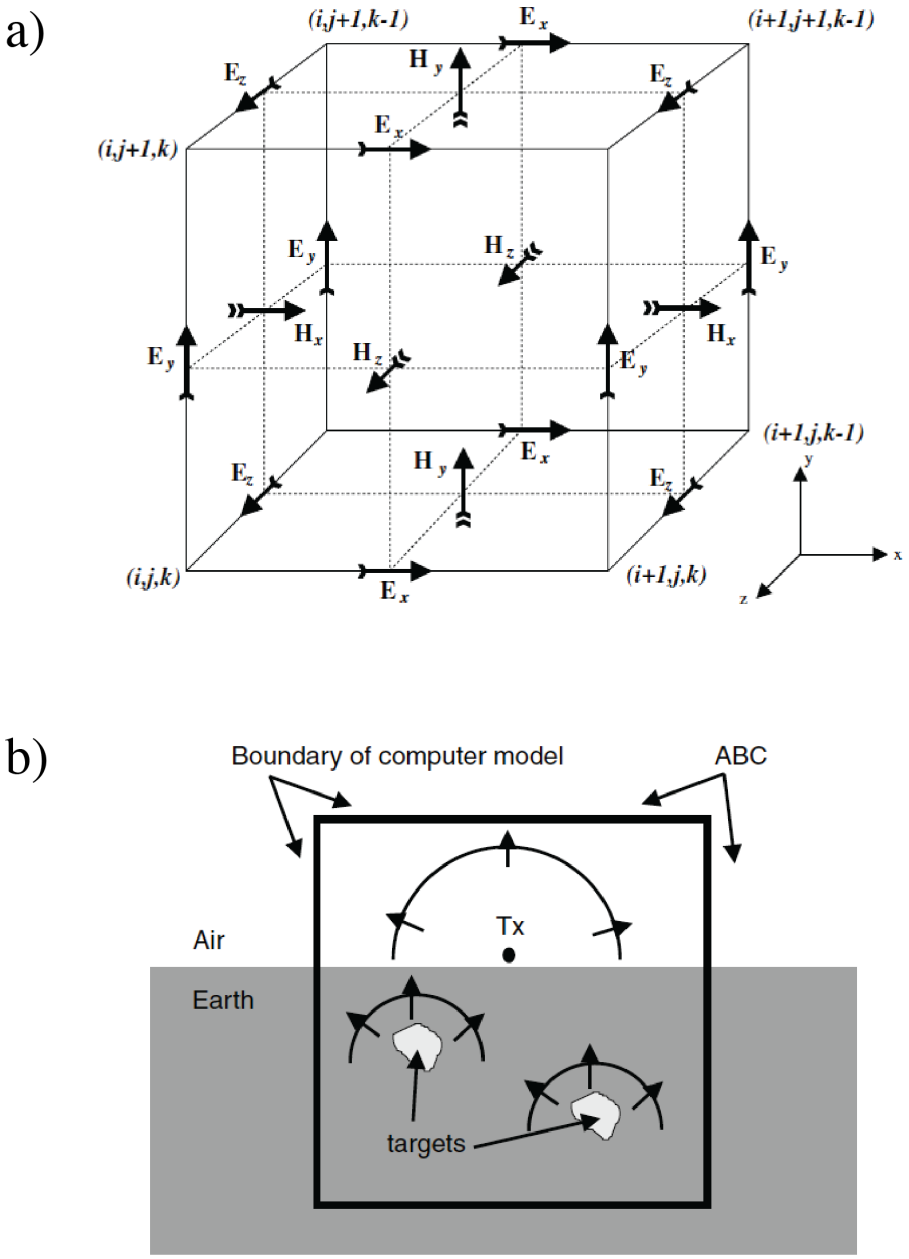

Figure 19: (a) The Yee cell which represents all the electric and magnetic vector field components on a 3D grid. (b) The cross-section representing an unbounded model in bounded space. If the boundaries are not ABC (absorbing boundary conditions) the model response will contain reflections of the targets off the boundary. This will create false diffractions in the data. (modified from Giannopoulos, 2005)

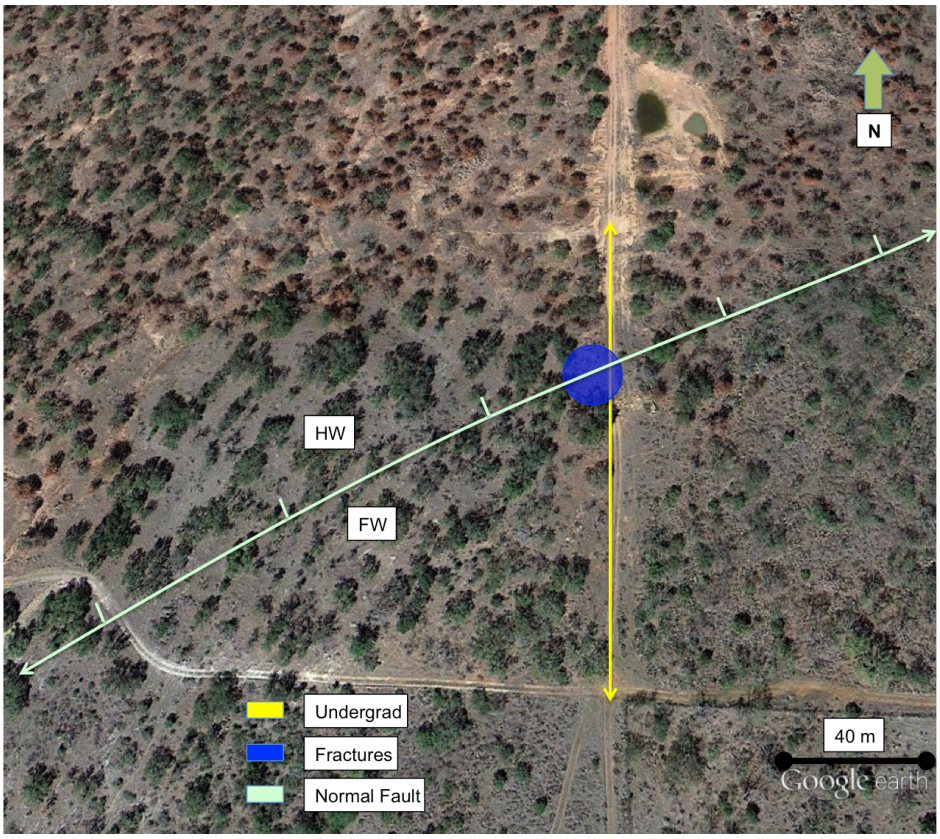

Figure 20: Aerial image showing the locations of the various GPR data acquisition with the approximate location of the fault in green (map image from Google Earth)

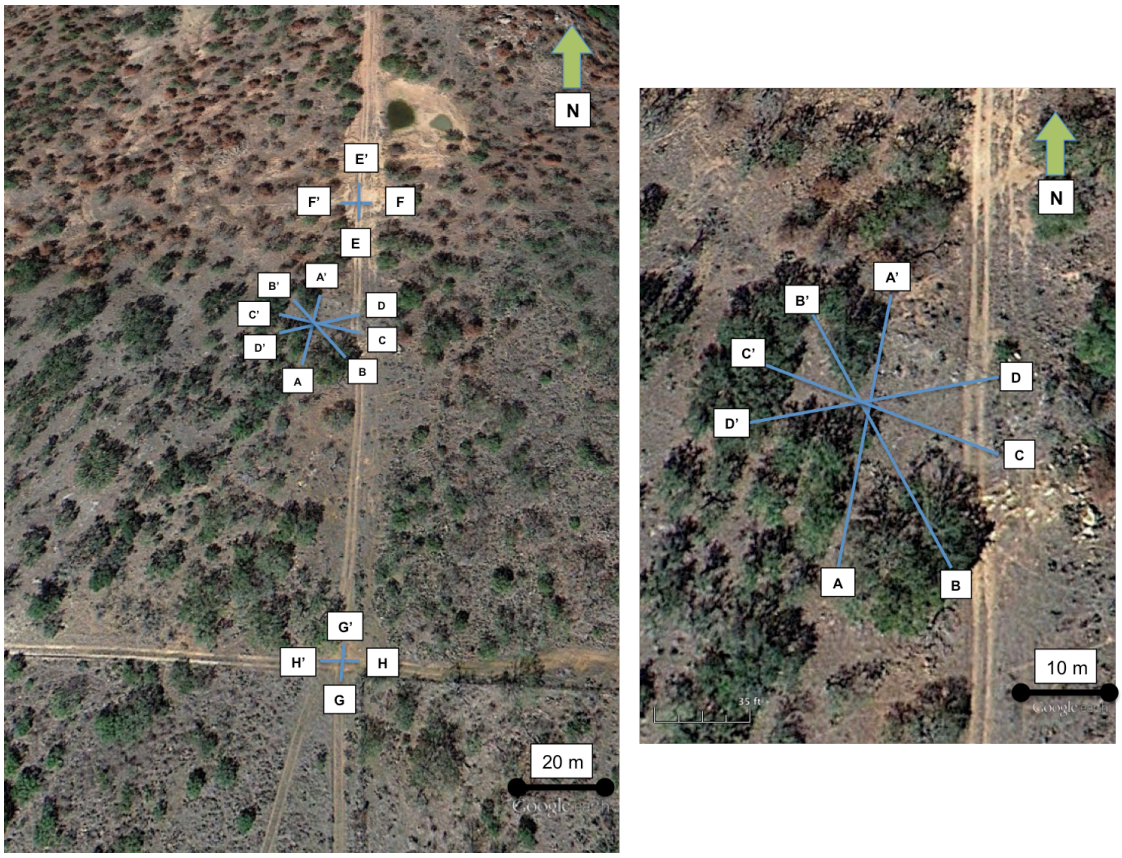

Figure 21: Aerial map of the field area for data acquisition for fracture characterization. Blue lines represent the approximate location of the survey lines. (image from Google Earth)

Figure 22: Picture of the field area. There were many obstacles such as boulders and various types of foliage limiting the acquisition of additional survey profiles.

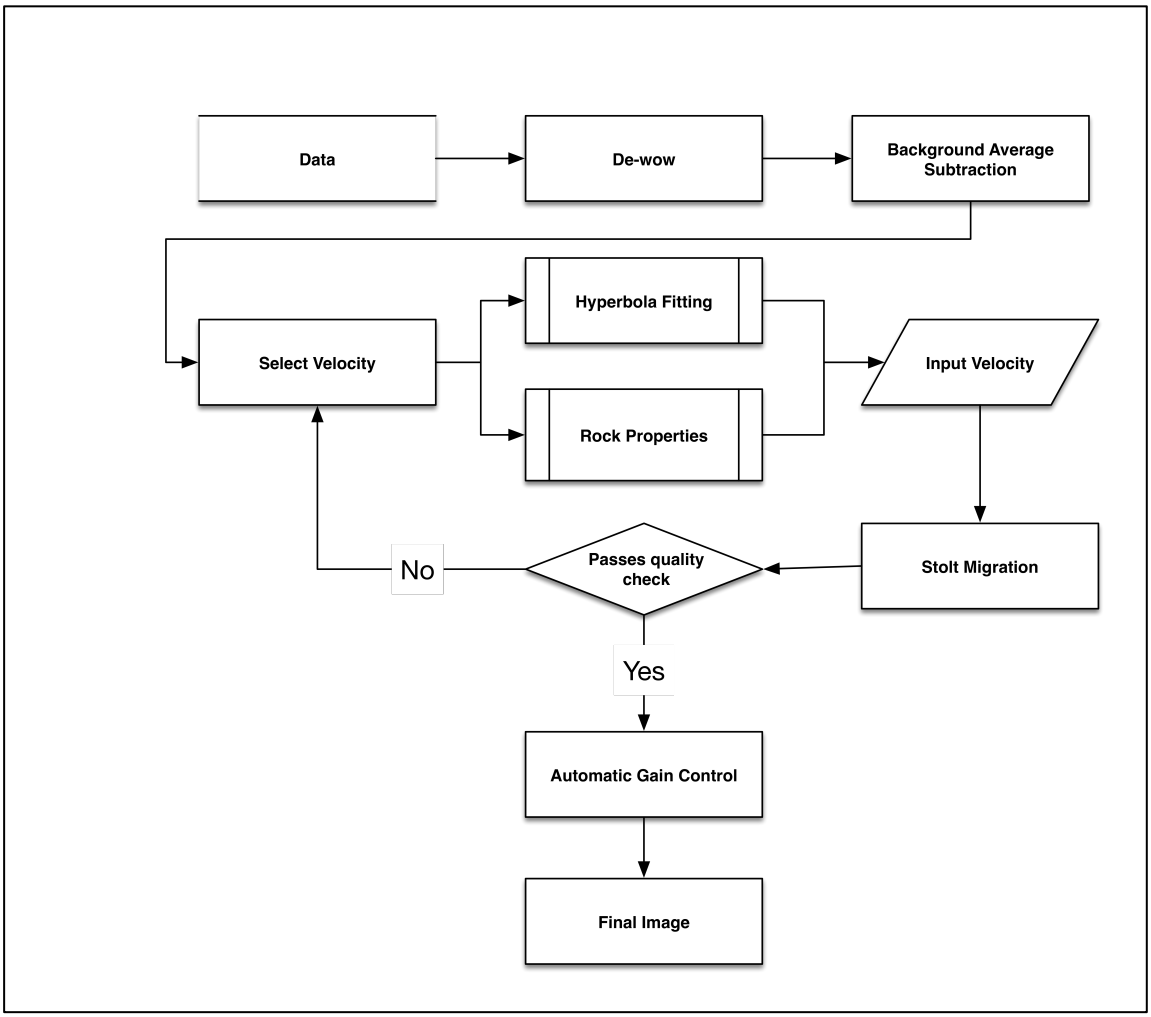

Figure 23: The processing workflow used for the multi-polarization multi-azimuthal GPR dataset.

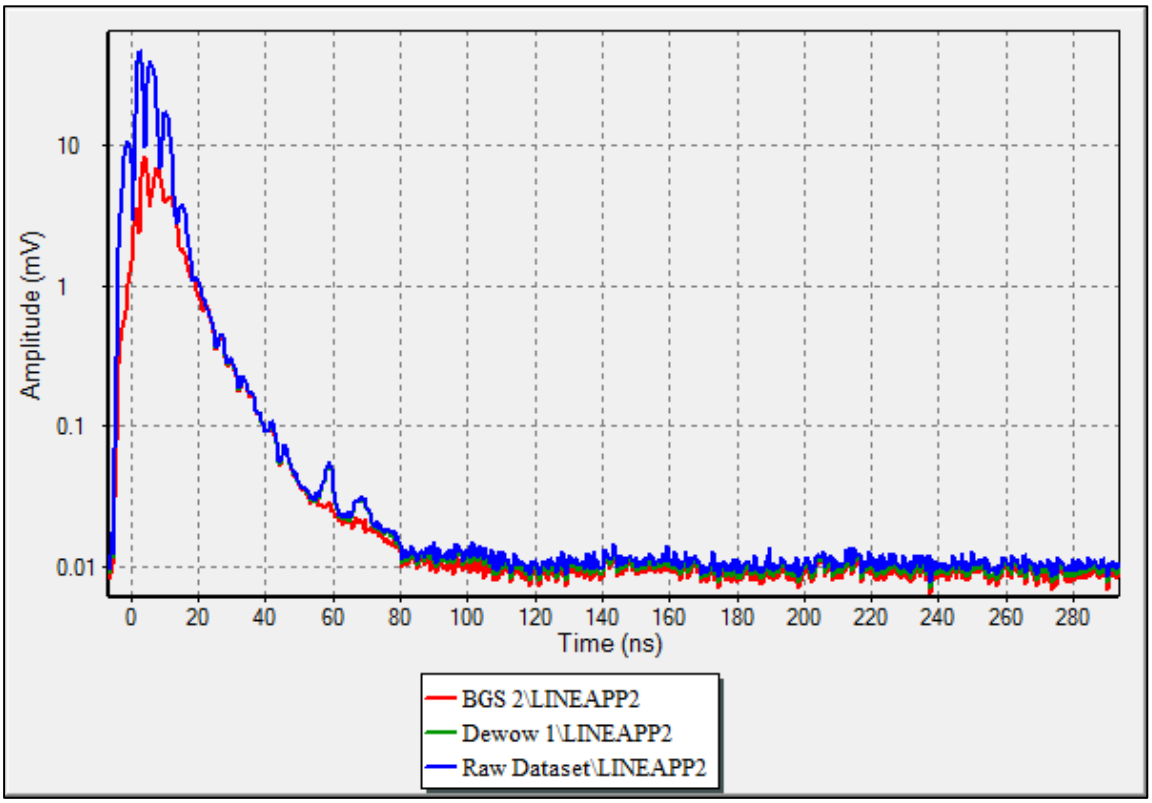

Figure 24: Amplitude vs Time chart showing the changes to the raw data after de-wow and background average subtractions has been applied. The chart is from the PulseEkko software.

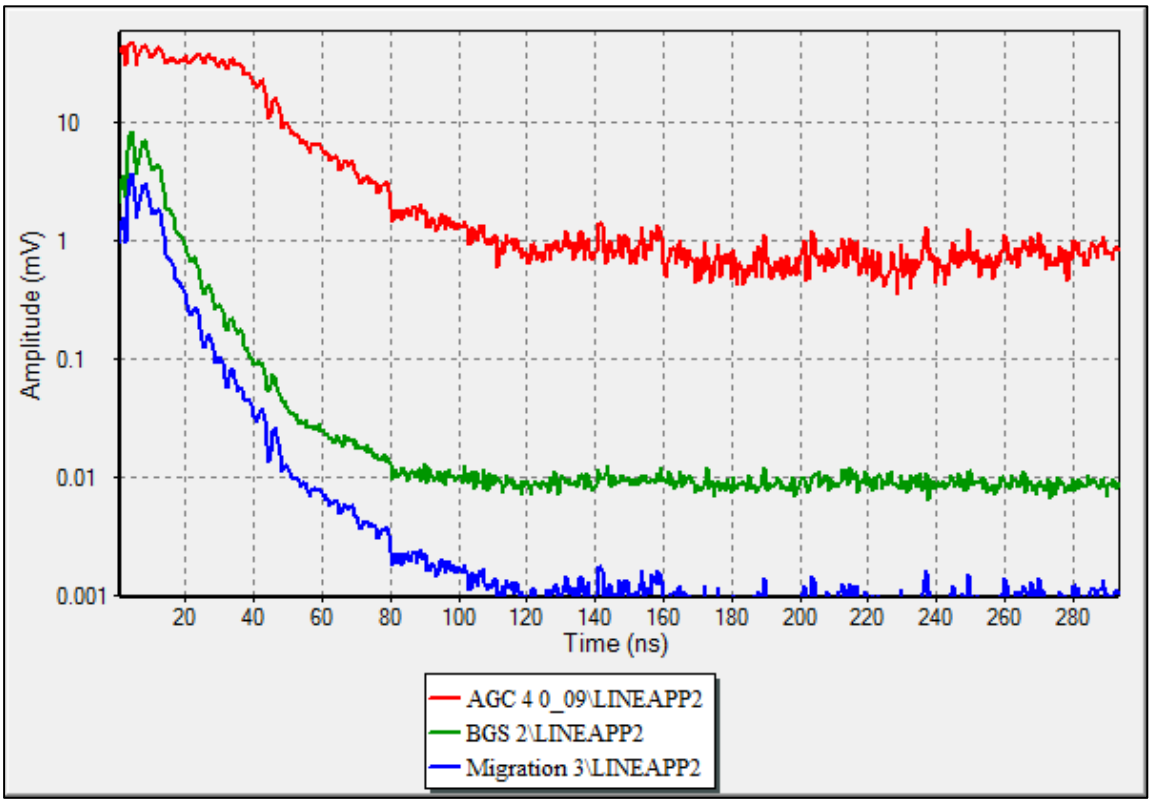

Figure 25: Amplitude vs Time chart showing the changes to background average subtractions after Stolt migration and AGC has been applied. The chart is from the PulseEkko software.

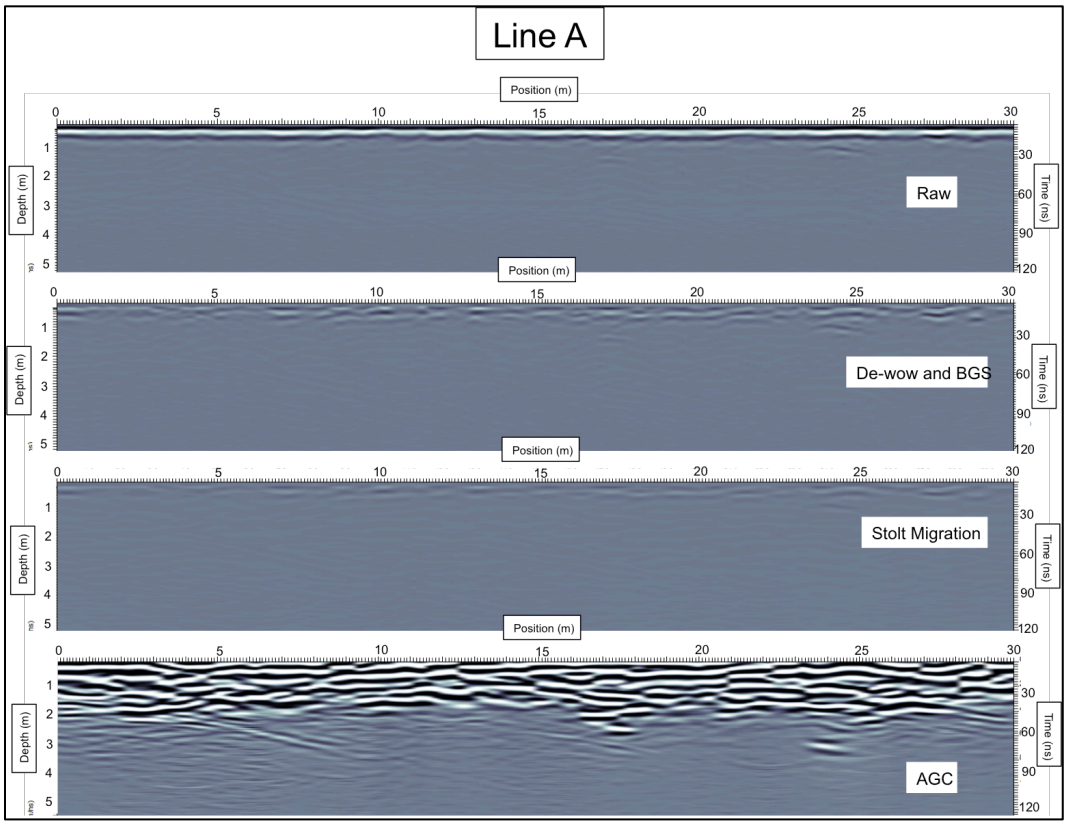

Figure 26: Line A PP at different stages of processing workflow.

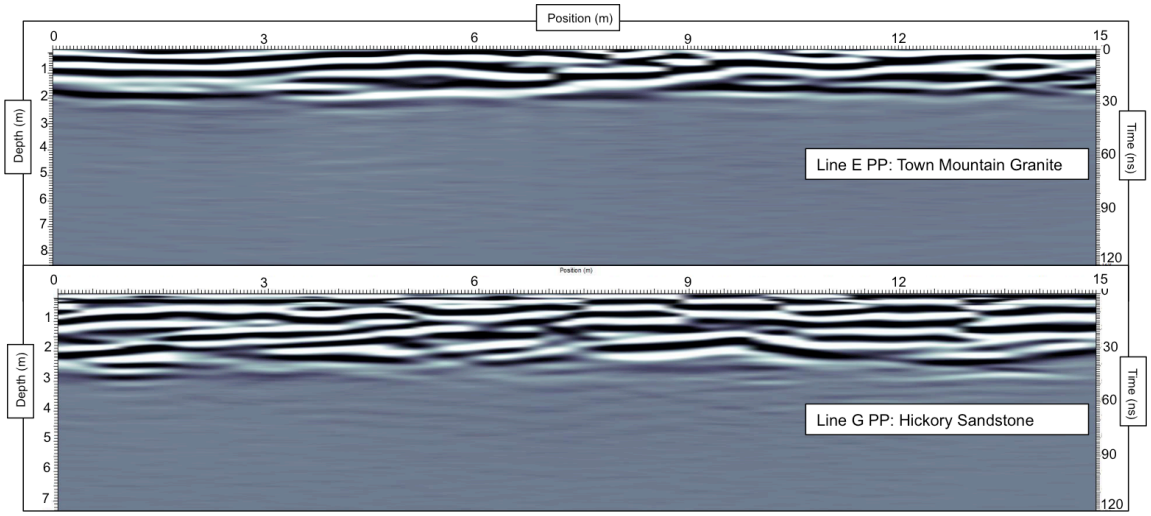

Figure 27: The top GPR line is the S-N line across the Town Mountain Granite. The bottom GPR line is the S-N Hickory Sandstone.

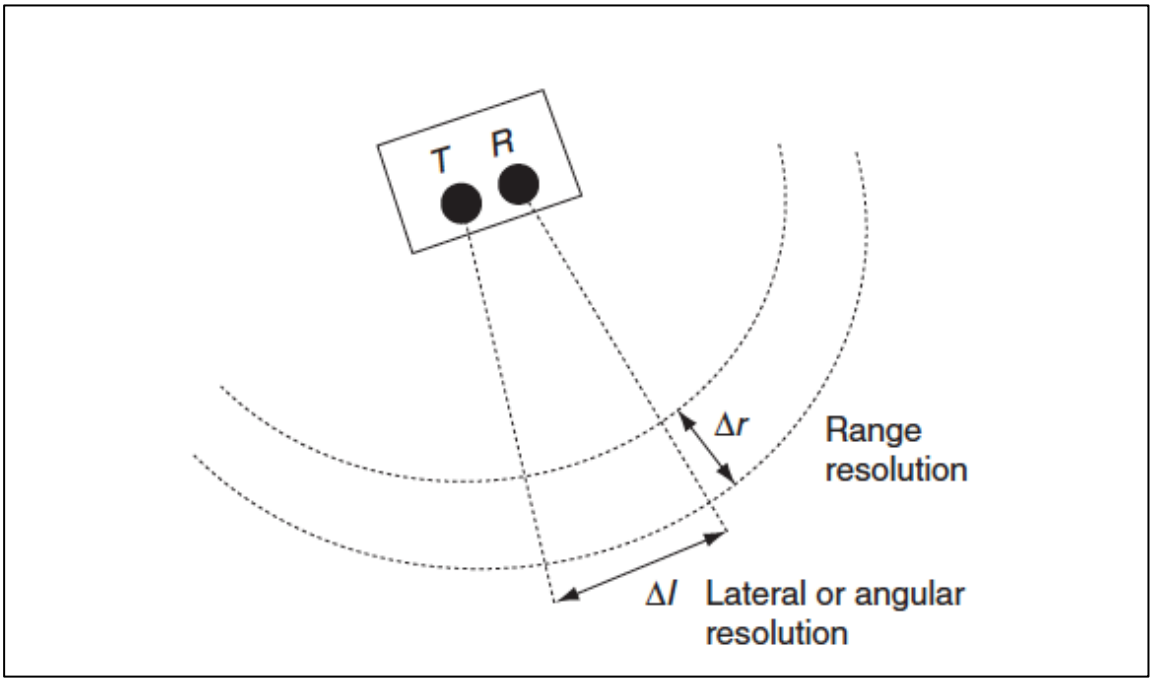

Figure 28: GPR resolution can be divided into two parts: range resolution (Vertical resolution) and later resolution (horizontal resolution). (Annan, 2009)

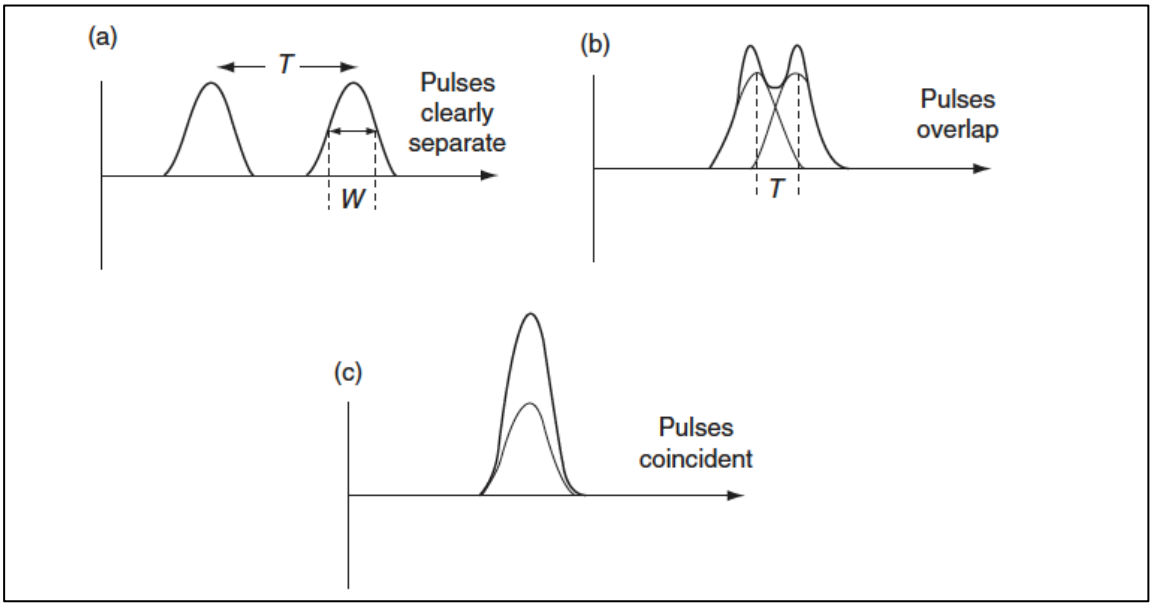

Figure 29: (a) The pulses are clearly separated when there is a clear difference between the pulse width and wavelength between the two pulses. (b) When the pulse width and the wavelength between the two pulses are similar, the pulses could be distinguishable until this point. After this, the two pulses will look like one. (c) Showing that when the wavelength between the two pulses is a lot smaller than the pulse width, the two pulses are not distinguishable. (Annan, 2009)

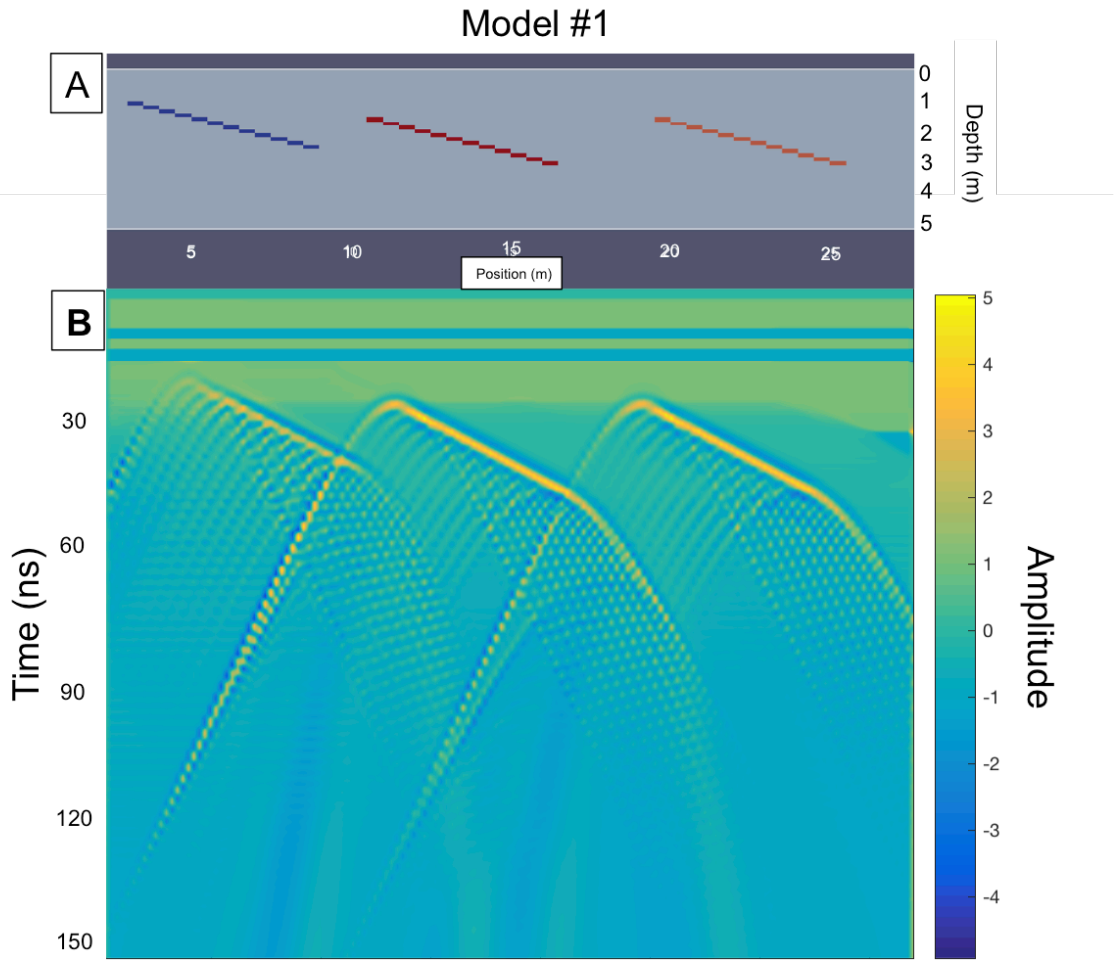

Figure 30: (a) The geometry of Model 1. Blue is air filled fracture. Red is clay filled fracture. Orange is water filled fracture. (b) Results of the 2-D FDTD method from gprMax. There is varying amplitude strength of the different fracture response.

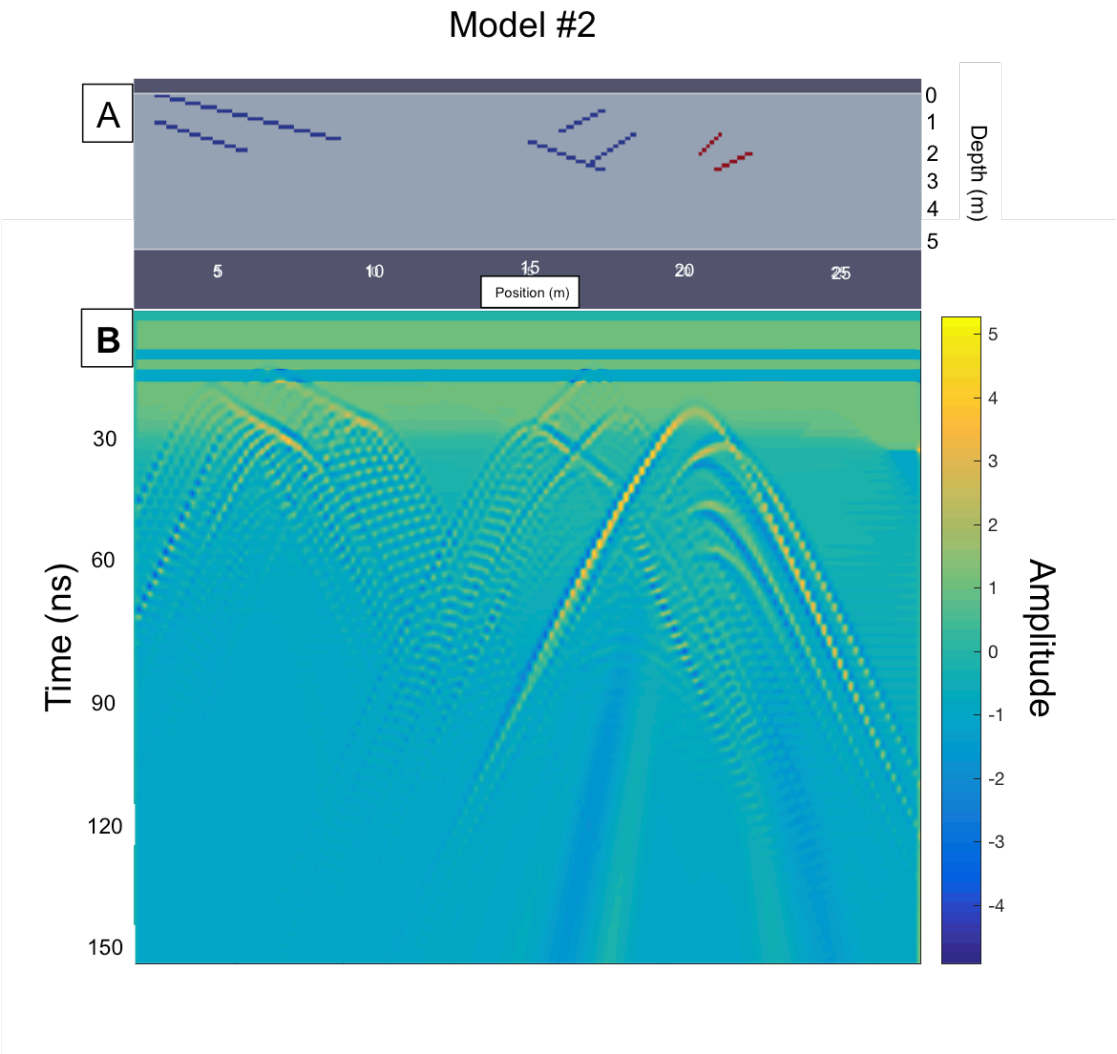

Figure 31: (A) The geometry of Model #2. Representing the dominant fractures present in Line A PP and TT orientations. Blue fractures are air filled while the red fractures are clay filled. (B) The results show that the air filled fractures are weaker while the clay filled fractures show stronger amplitude.

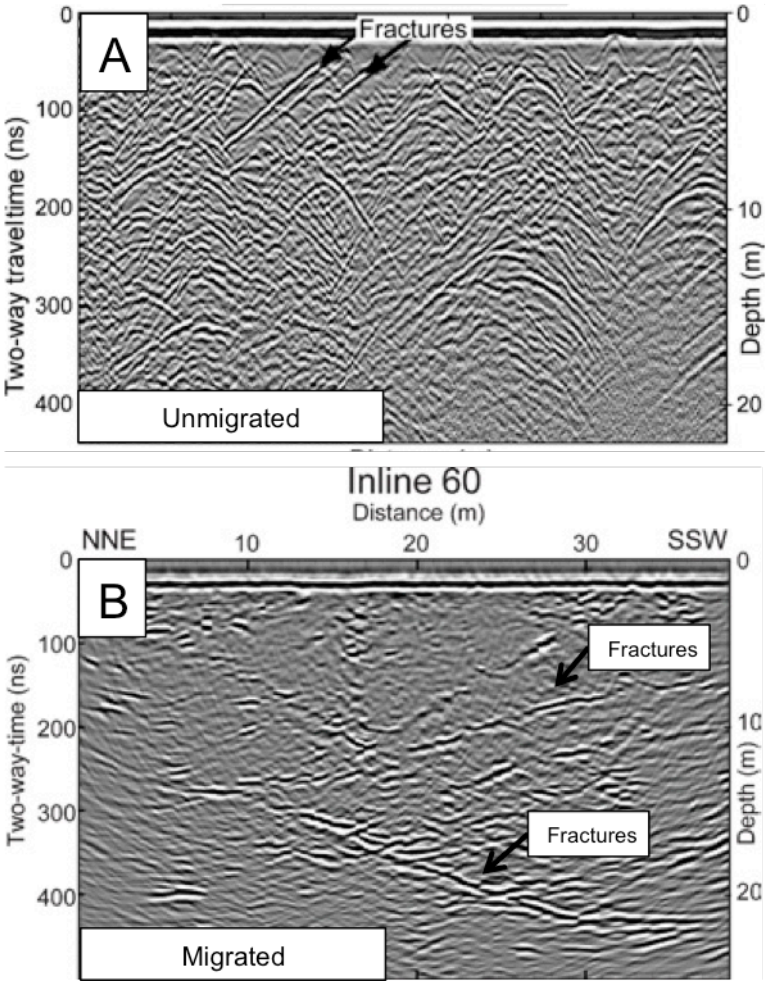

Figure 32: (A) A 2-D unmigrated time slice showing the various diffractions at a quarry. (B) A 2-D migrated time slice, showing the fractures as crosscutting features. (modified from Grasmueck et al., 2005)

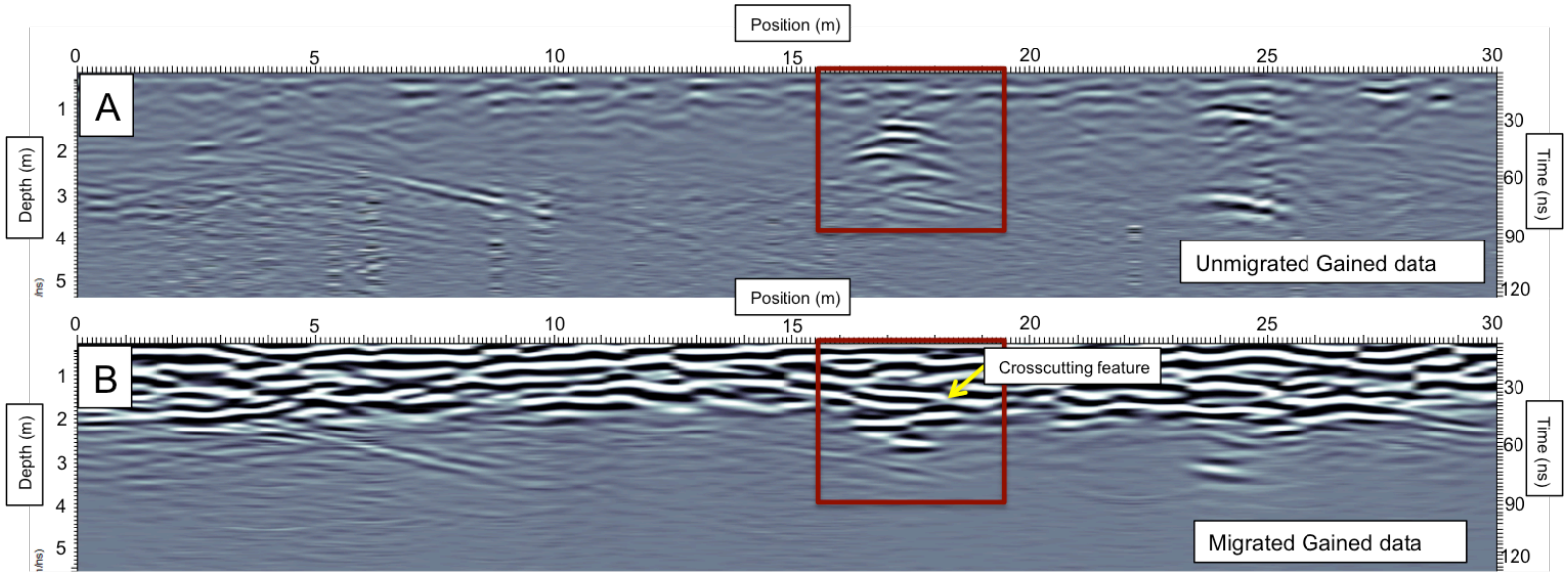

Figure 33: A and B are 2-D radar sections of Line A PP orientation at different processing steps. (A) Unmigrated gained 2-D line showing a series of diffractions, highlighted in red box. (B) Migrated gained 2-D line displaying the diffraction collapsed and representing a crosscutting feature.

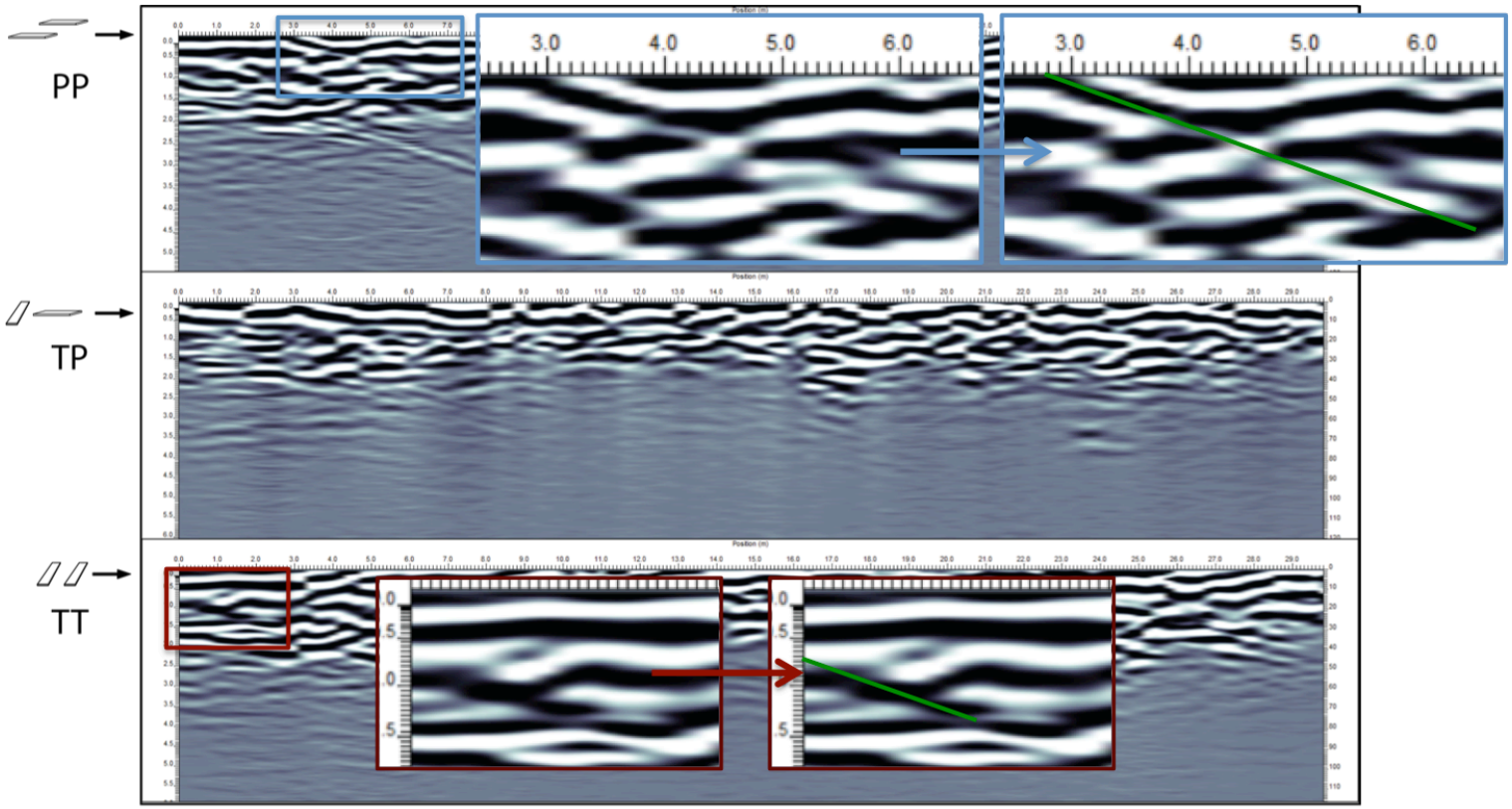

Figure 34: Figure displaying examples of the cross cutting features interpreted as fractures within the dataset

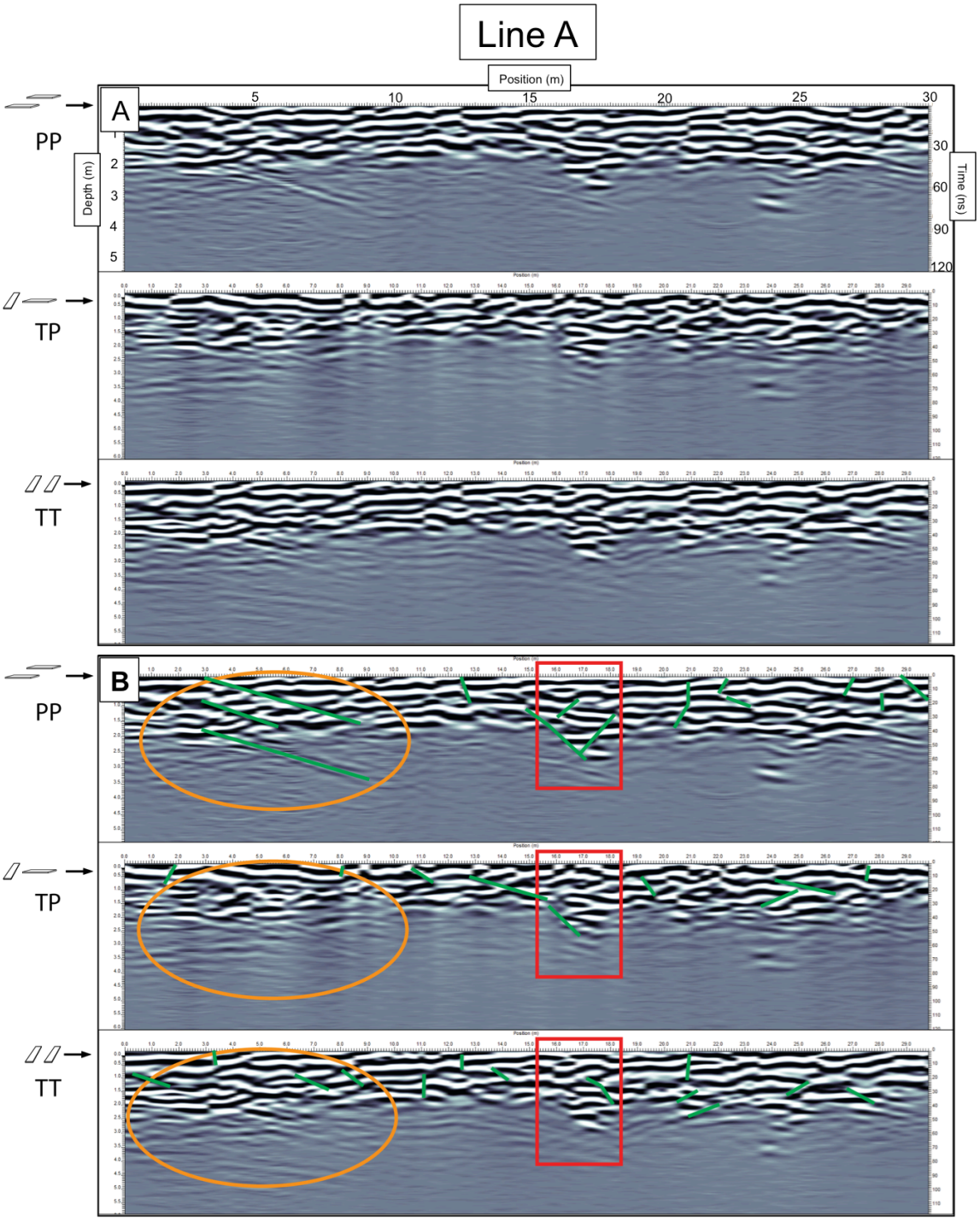

Figure 35: Line A with the 3 polarizations. (A) Uniterpreted data. (B) The green lines are interpreted as fractures. The orange ellipse is highlighting the different fractures interpreted in the different orientations. The red box is highlighting the fault core location.

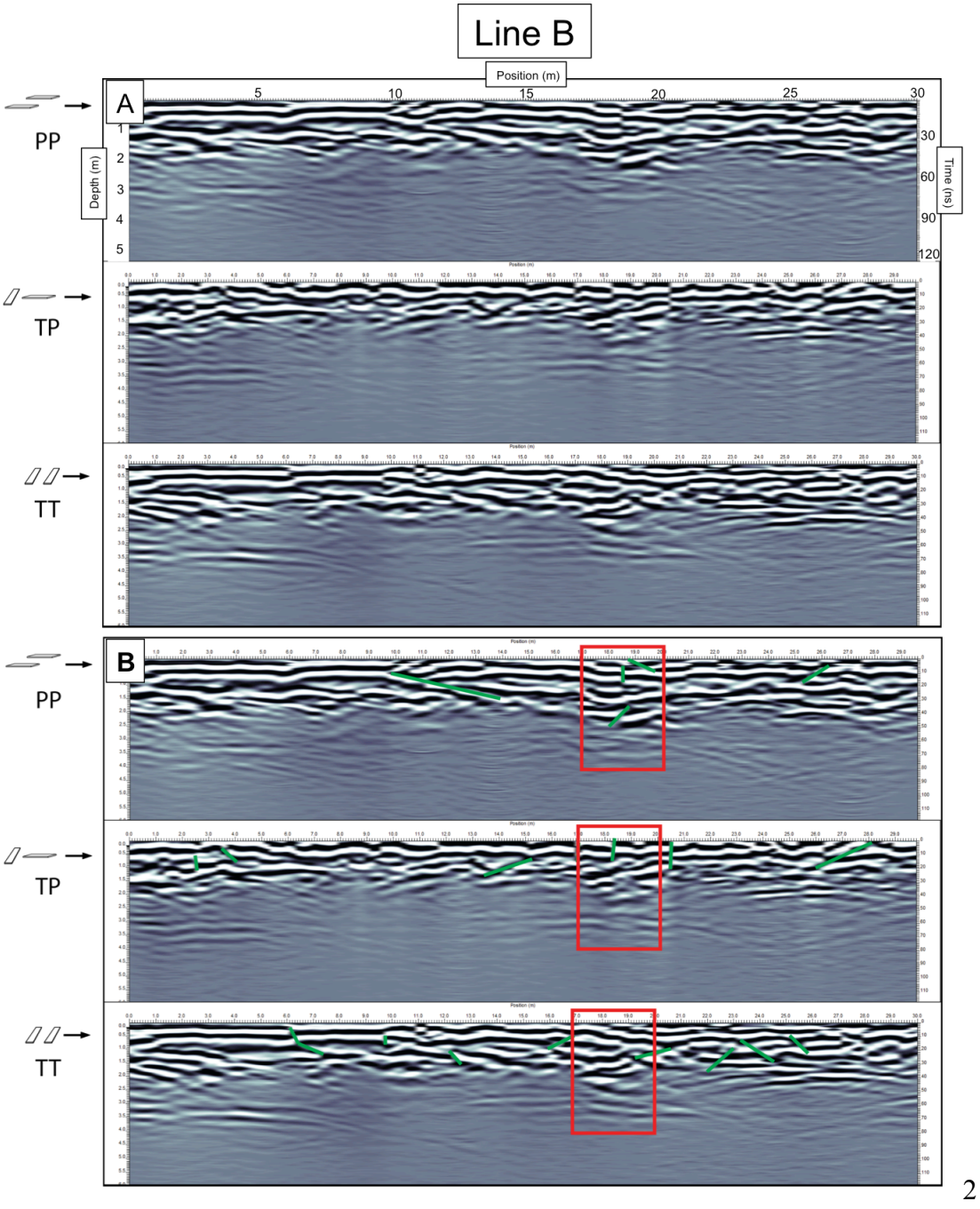

Figure 36: Line B with the 3 polarizations. (A) Uninterpreted data. (B) The green lines represent fractures. The red box is highlighting the fault core.

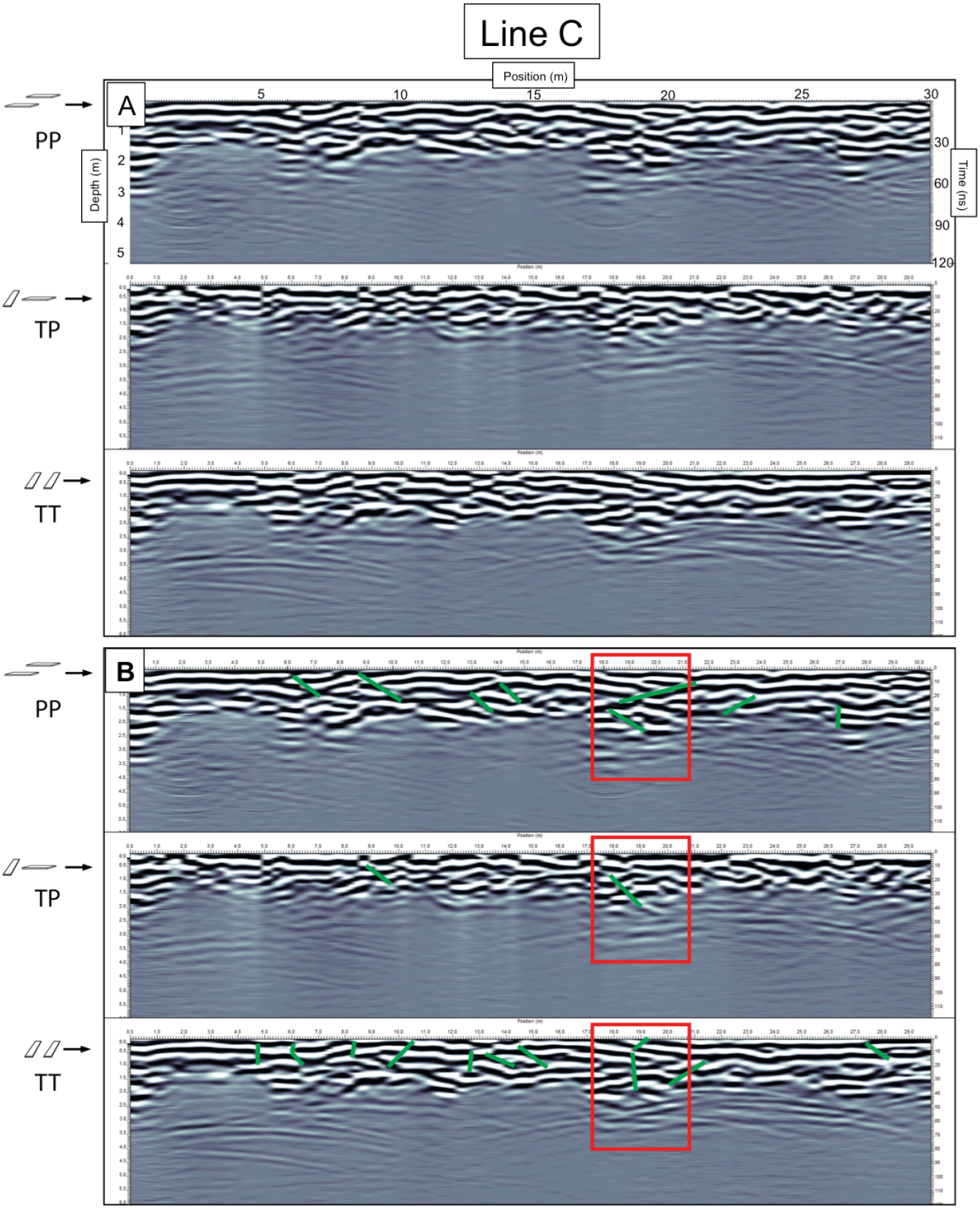

Figure 37: Line C with 3 polarizations. There a lot of variation on depth of penetration, indicating more folding of units is present. (A) Uninterpreted data. (B) The green lines represent fractures while the red box is highlighting the fault core.

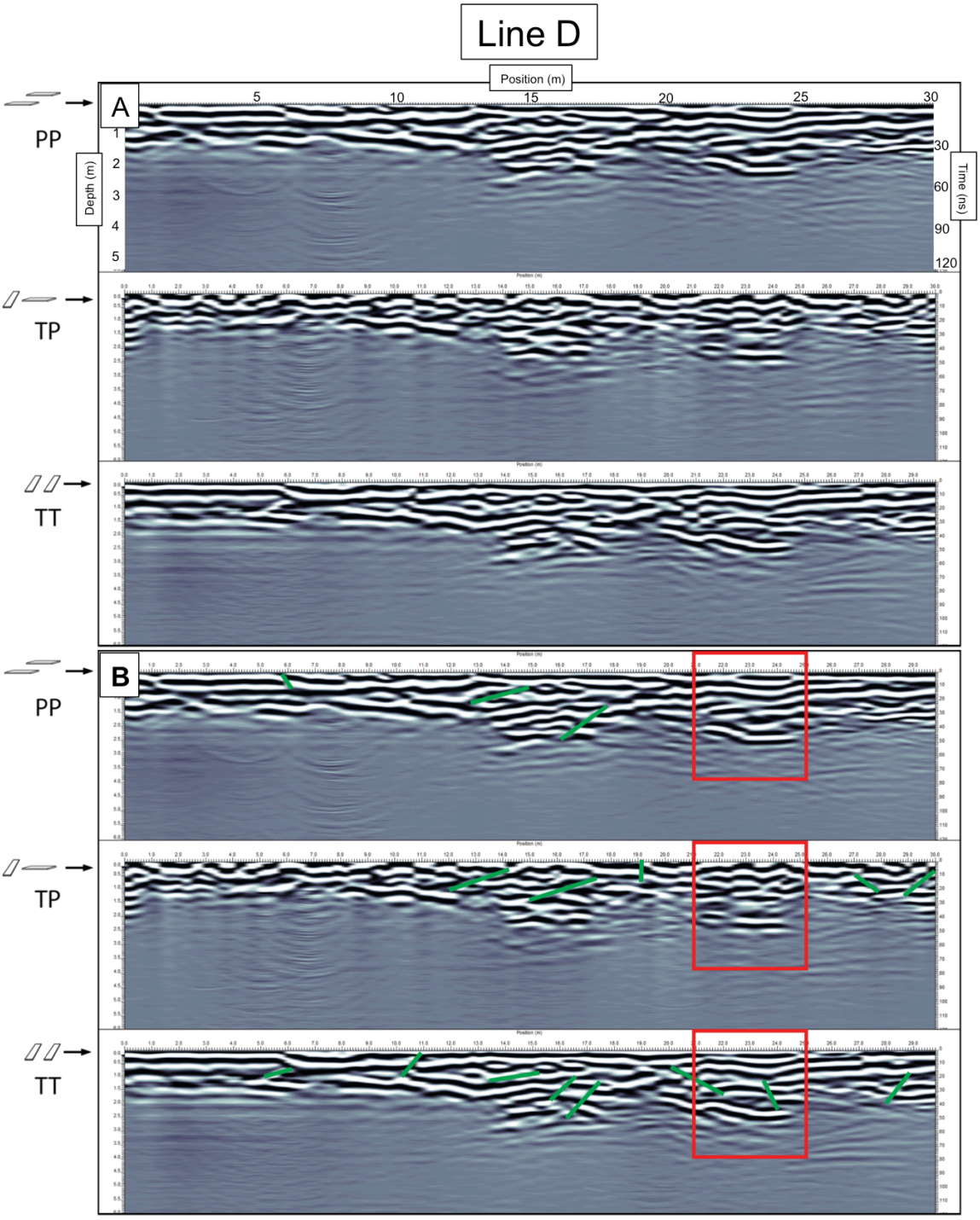

Figure 38: Line D with 3 polarizations. (A) Uninterpreted data. (B) The green lines represent fractures while the red box is highlighting the fault core.

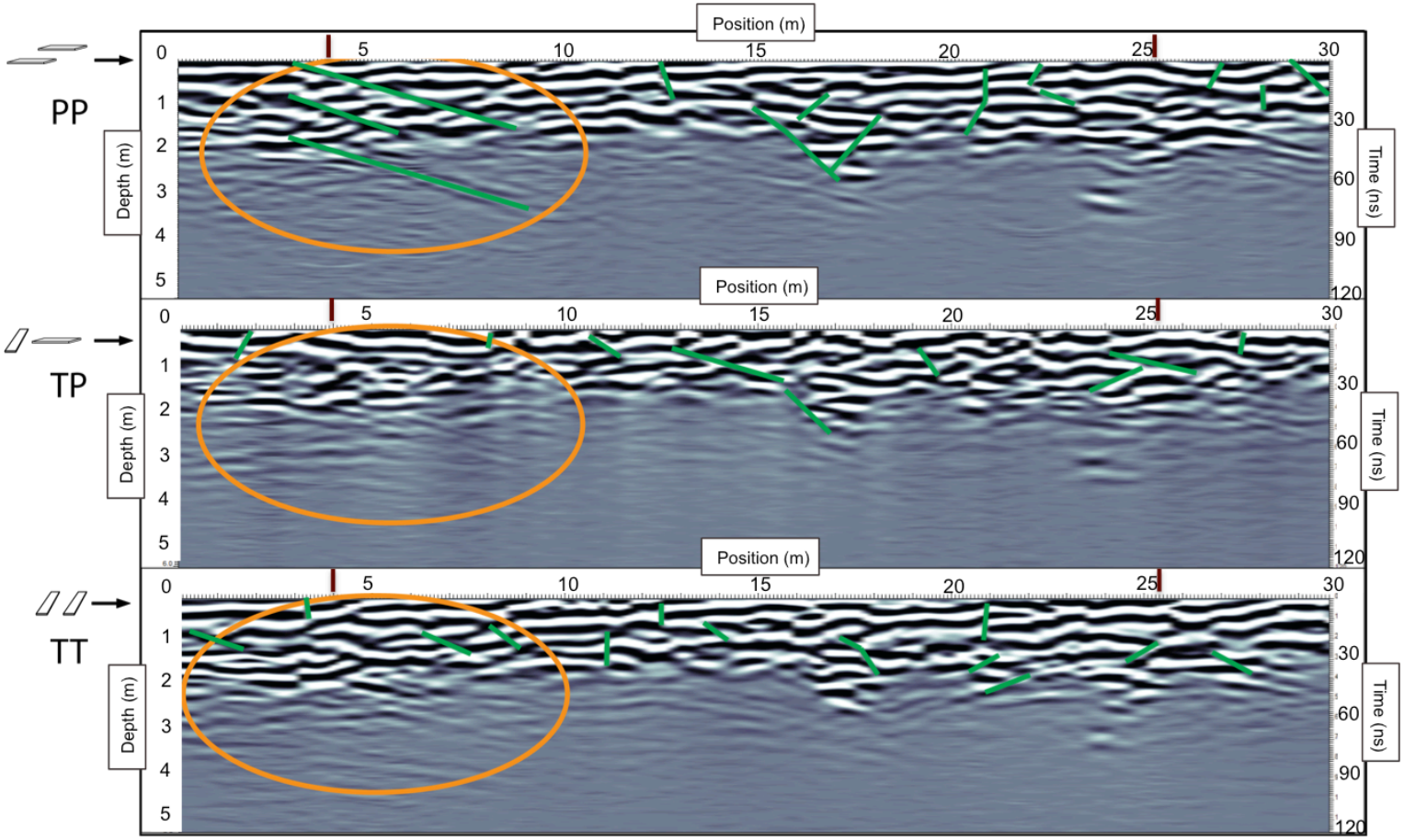

Figure 39: The orange circle highlighting different fractures seen in different polarizations along the same survey Line A.

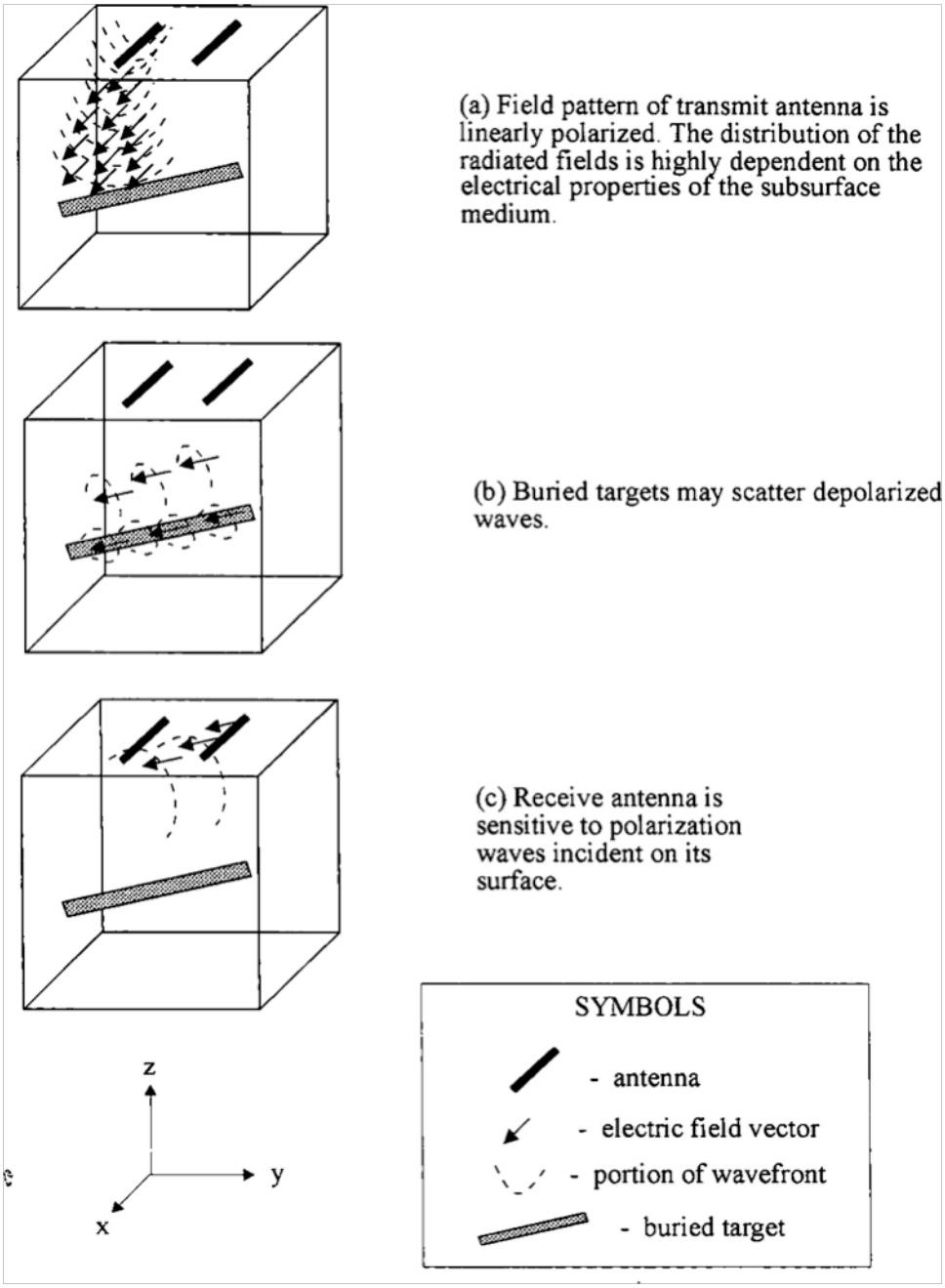

Figure 40: A schematic diagram showing step by step of the propagation and response of the electric field. (Roberts and Daniels, 1996)

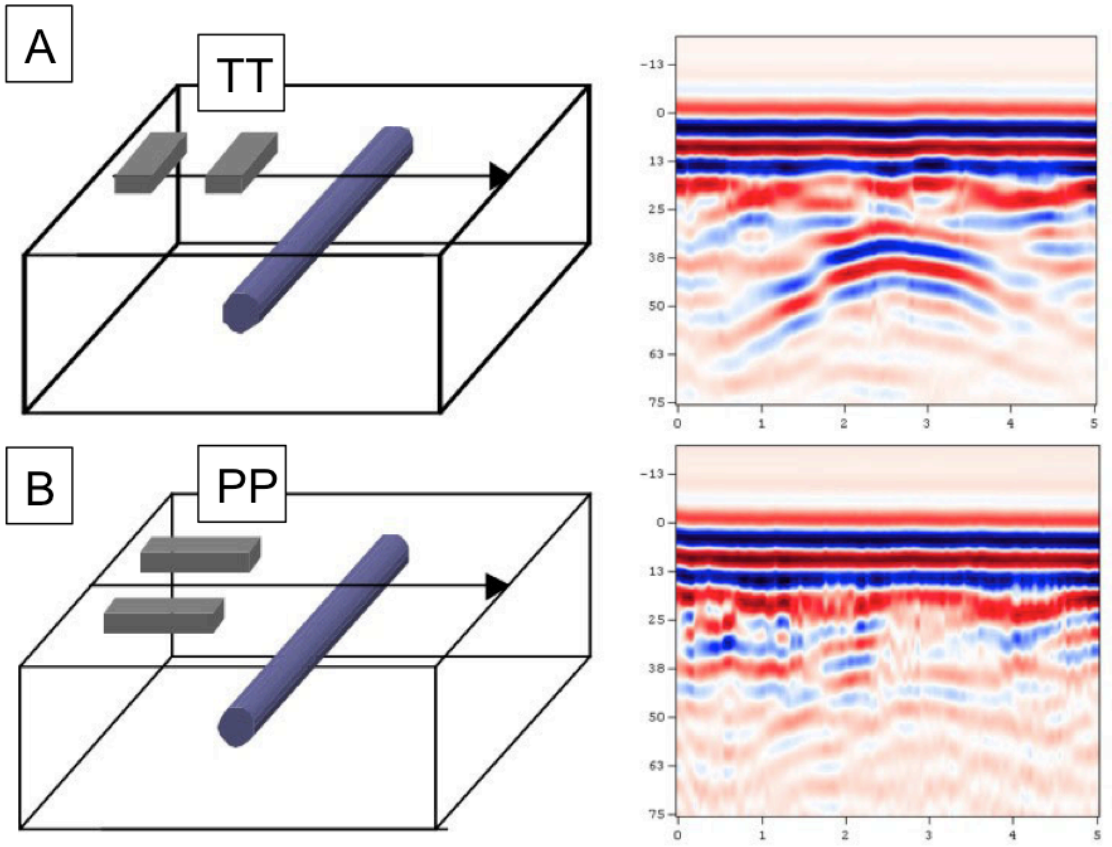

Figure 41: A GPR survey over a buried water filled pipe. TT orientation is able to detect the pipe while the PP orientation does not. (modified from Grasmueck et al., 2005)

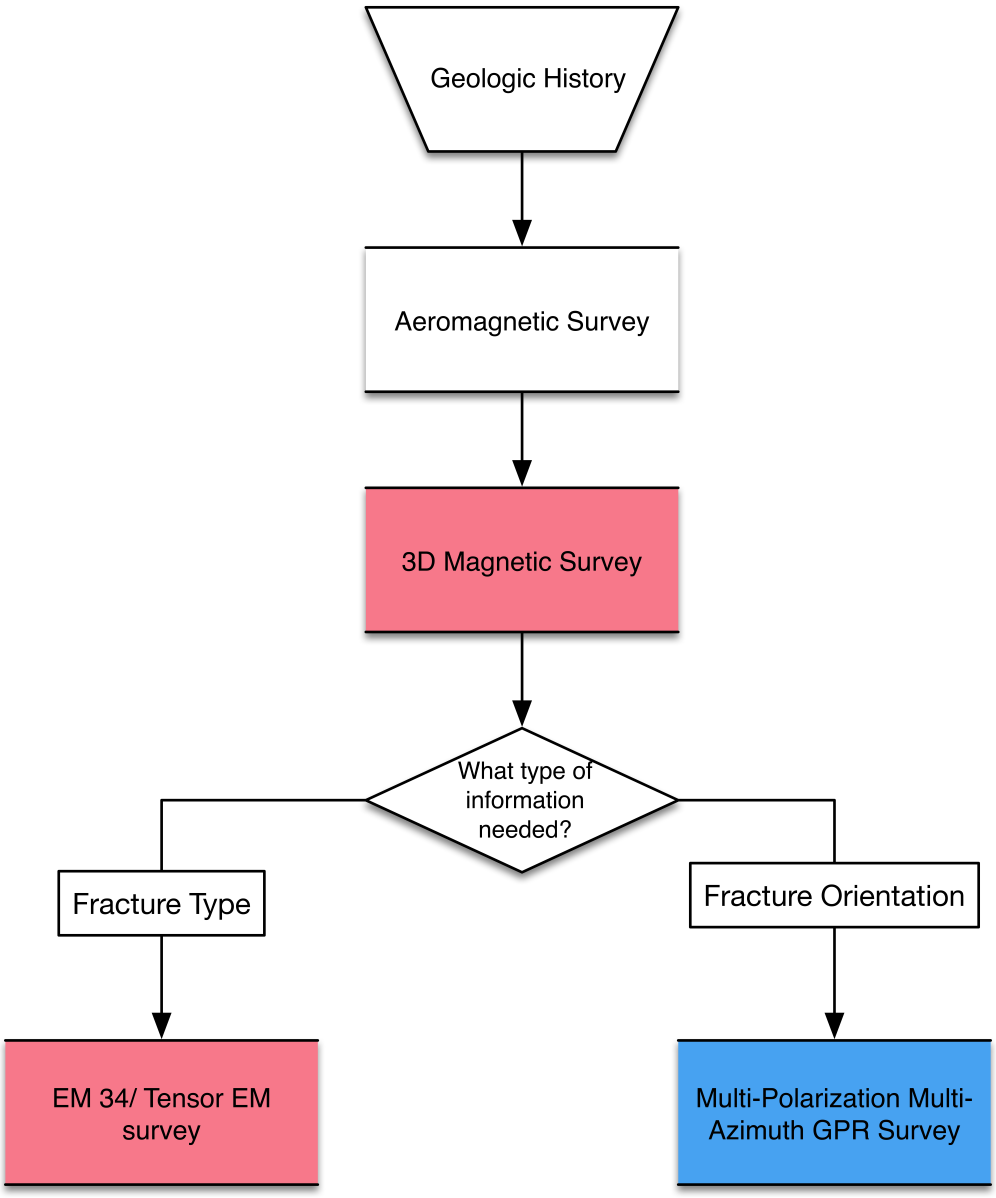

Figure 42: A workflow designed to help find shallow buried faults and help characterize the fault zone.

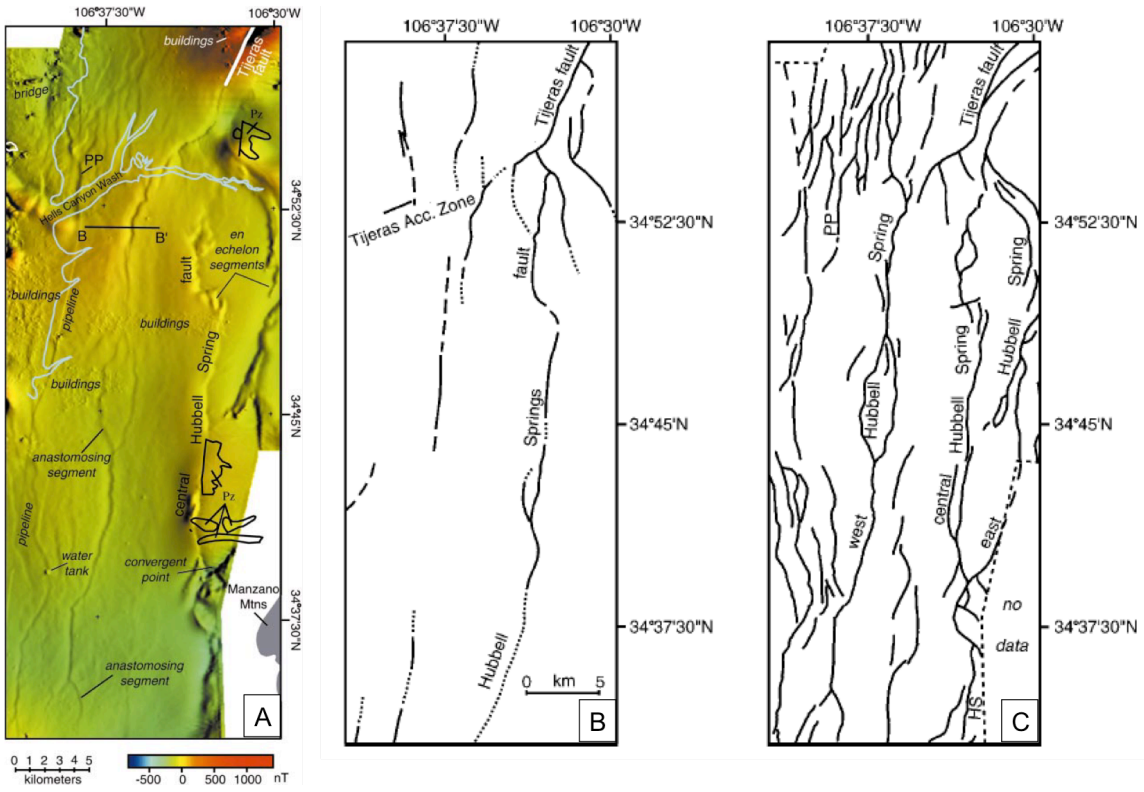

Figure 43: (A) An Aeromagnetic image that is color coded to show relief. The relief is caused due to the faults. (B) Faults that were mapped previously by other researchers. (C) Faults inferred from the aeromagnetic map shown in part A. (modified from Grauch, 2001)

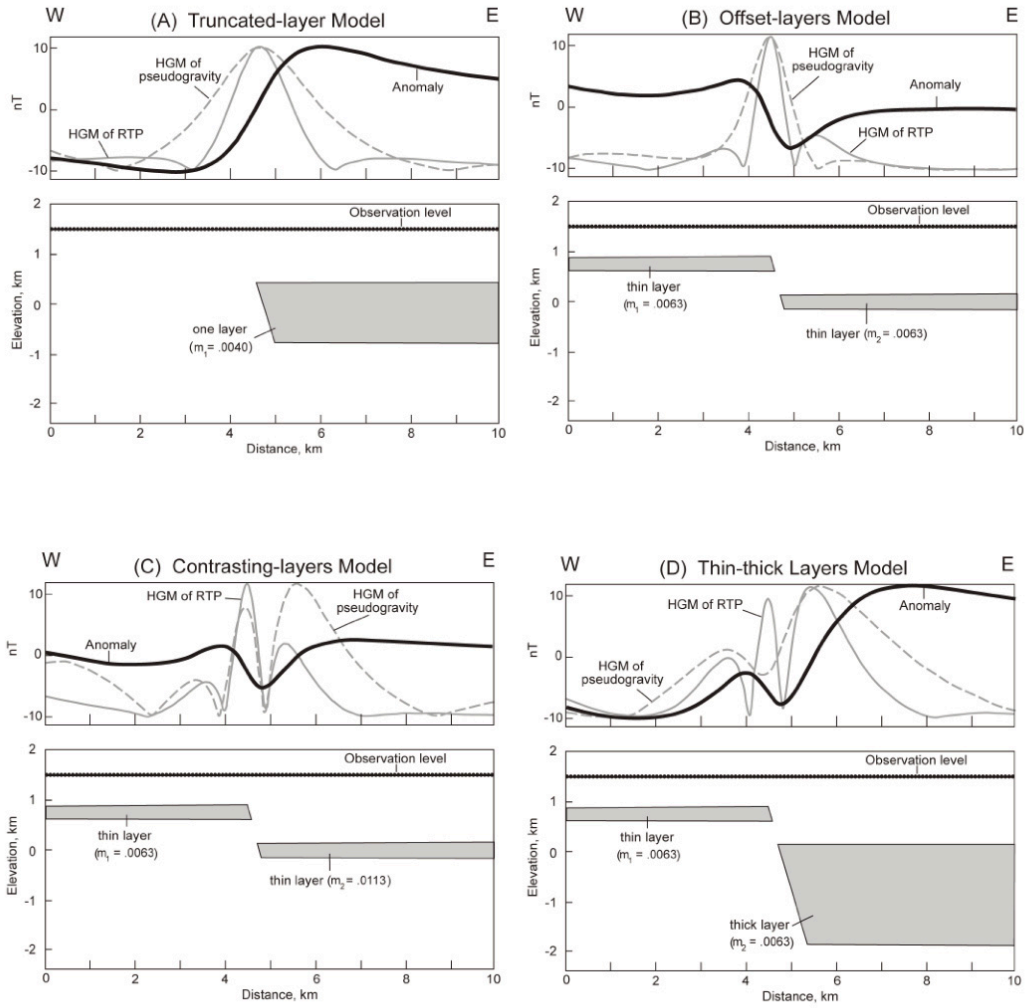

Figure 44: Geophysical models simulating different survey across different types of faults. All four models show a clear magnetic anomaly at the location of the fault. (Howell, 2010)

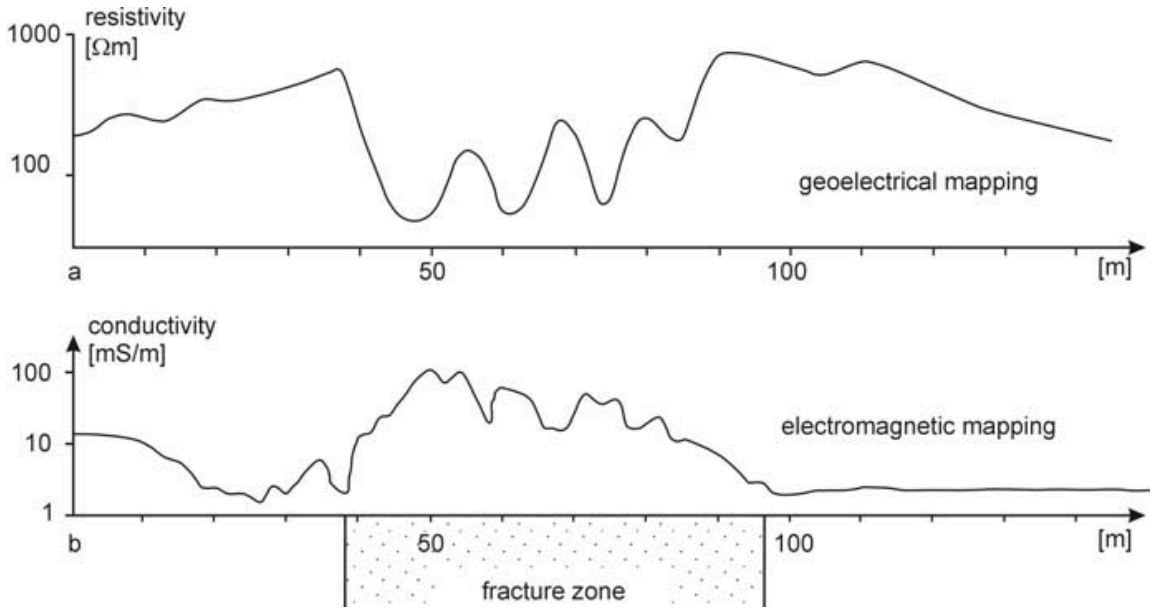

Figure 45: A geoelectrical survey and EM 31 survey for mapping n open water-filled fracture zone. Due to this the fracture zone has low resistivity or high conductivity. This is seen in the data. The electrical survey measured the resistivity of the rocks and had a low response over the fractured zone. While the EM 31 was measuring the conductivity, had a high response over the fracture zone. (Ernstson and Kirsch, 2006)